Calculation of prompt diphoton production cross sections at Tevatron and LHC energies

C. Balázs[1],[*] E. L. Berger[1],[†] P. Nadolsky[1],[‡] and C.-P. Yuan[2][§]

[1]*High Energy Physics Division, Argonne National Laboratory, Argonne, IL 60439*
[2]*Department of Physics and Astronomy,*
Michigan State University, East Lansing, MI 48824
(Dated: May 3, 2007)

Abstract

A fully differential calculation in perturbative quantum chromodynamics is presented for the production of massive photon pairs at hadron colliders. All next-to-leading order perturbative contributions from quark-antiquark, gluon-(anti)quark, and gluon-gluon subprocesses are included, as well as all-orders resummation of initial-state gluon radiation valid at next-to-next-to-leading logarithmic accuracy. The region of phase space is specified in which the calculation is most reliable. Good agreement is demonstrated with data from the Fermilab Tevatron, and predictions are made for more detailed tests with CDF and DØ data. Predictions are shown for distributions of diphoton pairs produced at the energy of the Large Hadron Collider (LHC). Distributions of the diphoton pairs from the decay of a Higgs boson are contrasted with those produced from QCD processes at the LHC, showing that enhanced sensitivity to the signal can be obtained with judicious selection of events.

[*]balazs@hep.anl.gov; Current address: School of Physics, Monash University, Melbourne VIC 3800, Australia
[†]berger@anl.gov
[‡]nadolsky@hep.anl.gov
[§]yuan@pa.msu.edu

I. INTRODUCTION

The long-sought Higgs boson(s) h of electroweak symmetry breaking in particle physics may soon be observed at the CERN Large Hadron Collider (LHC) through the diphoton decay mode ($h \rightarrow \gamma\gamma$). Purely hadronic standard model processes are a copious source of diphotons, and a narrow Higgs boson signal at relatively low masses will appear as a small peak above this considerable background. A precise theoretical understanding of the kinematic distributions for diphoton production in the standard model could provide valuable guidance in the search for the Higgs boson signal and assist in the important measurement of Higgs boson coupling strengths.

In this paper we address the theoretical calculation of the invariant mass, transverse momentum, rapidity, and angular distributions of continuum diphoton production in proton-antiproton and proton-proton interactions at hadron collider energies. We compute all contributions to diphoton production from parton-parton subprocesses through next-to-leading order (NLO) in perturbative quantum chromodynamics (QCD). These higher-order contributions are large at the LHC, and their inclusion is mandatory for quantitatively trustworthy predictions. We resum initial-state soft and collinear logarithmic terms associated with gluon radiation to all orders in the strong coupling strength α_s. This resummation is essential for physically meaningful predictions of the transverse momentum (Q_T) distribution of the diphotons at small and intermediate values of Q_T, where the cross section is large. In addition, we analyze the final-state collinearly-enhanced contributions, also known as 'fragmentation' contributions, in which one or both photons are radiated from final-state partonic constituents. We compare the results of our calculations with data on isolated diphoton production from the Fermilab Tevatron [1]. The good agreement we obtain with the Tevatron data adds confidence to our predictions at the energy of the LHC. The present work expands on our recent abbreviated report [2], and it may be read in conjunction with our detailed treatment of the contributions from the gluon-gluon subprocess [3].

Our attention is focused on the production of isolated photons, *i.e.*, high-energy photons observed at some distance from appreciable hadronic remnants in the particle detector. The rare isolated photons tend to originate directly in hard QCD scattering, in contrast to copiously produced non-isolated photons that arise from nonperturbative processes such as π and η decays, or from via quasi-collinear radiation off final-state quarks and gluons.

We evaluate contributions to continuum diphoton production from the basic short-distance channels for $\gamma\gamma$ production initiated by quark-antiquark and (anti)quark-gluon scattering, as well as by gluon-gluon and gluon-(anti)quark scattering proceeding through a fermion-loop diagram. At lowest order in QCD, a photon pair is produced from $q\bar{q}$ annihilation [Fig. 1 (a)]. Representative next-to-leading order (NLO) contributions to $q\bar{q} + qg$ scattering are shown in Fig. 1 (b)-(e). They are of $\mathcal{O}(\alpha_s)$ in the strong coupling strength [4, 5]. Production of $\gamma\gamma$ pairs via a box diagram in gg scattering [Fig. 1 (h)] is suppressed by two powers of α_s compared to the lowest-order $q\bar{q}$ contribution, but it is enhanced by a product of two large gluon parton distribution functions (PDFs) if typical momentum fractions x are small [6]. The $\mathcal{O}(\alpha_s^3)$ or NLO corrections to gg scattering include one-loop $gg \rightarrow \gamma\gamma g$ diagrams (i) and (j) derived in Ref. [7, 8], as well as 4-leg two-loop diagrams (l) computed in Ref. [9, 10]. In this study we also include subleading contributions from the process (k), $gq_S \rightarrow \gamma\gamma q_S$ via the quark loop, where $q_S = \sum_{i=u,d,s,...}(q_i + \bar{q}_i)$ denotes the flavor-singlet combination of quark scattering channels.
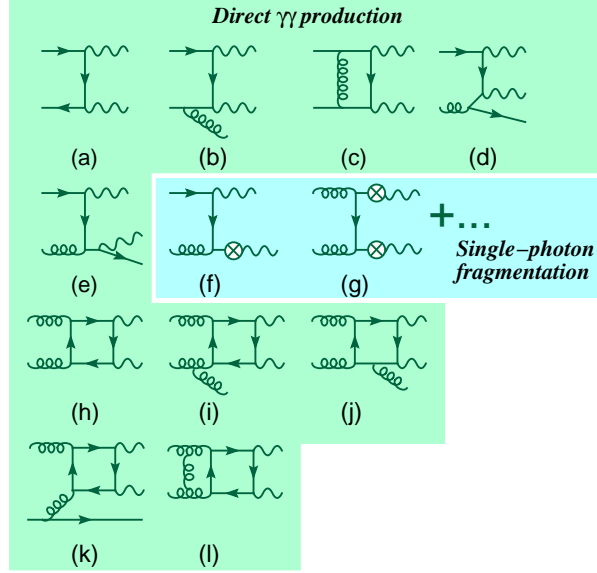
Figure 1: Representative partonic subprocesses that contribute to continuum diphoton production. All leading-order and next-to-leading order direct production subprocesses, i.e., contributions (a)-(e) and (h)-(l), are included in this study. Diagrams (f) and (g) are examples of single-photon one- and two-fragmentation.

Factorization is a central principle of hadronic calculations in perturbative QCD, in which a high-energy scattering cross section is expressed as a convolution of a perturbative partonic cross section with nonperturbative parton distribution functions (PDFs), thus separating short-distance from long-distance physics. The common factorization is a longitudinal notion, in the sense that the convolution is an integral over longitudinal momentum fractions, even if some partons in the hard-scattering process have transverse momenta that border the nonperturbative regime. Unphysical features may then arise in the transverse momentum (Q_T) distribution of a color-neutral object with high invariant mass (Q), such as a pair of photons produced in hadron-hadron collisions. When calculated in the common factorization approach at any finite order in perturbation theory, this distribution diverges as $Q_T \to 0$, signaling that infrared singularities associated with $Q_T \to 0$ have not been properly isolated and regulated. These singularities are associated with soft and collinear radiation from initial-state partons shown by the diagrams in Figs. 1 (b), (d), and (i).

A generalized factorization approach that correctly describes the small-Q_T region was developed by Collins, Soper, and Sterman (CSS) [11] and applied to photon pair production [7, 12, 13]. In this approach the hadronic cross section is expressed as an integral over the transverse coordinate (impact parameter). The integrable singular functions present in the finite-order differential distribution as $Q_T \to 0$ are resummed, to all orders in the strong coupling α_s, into a Sudakov exponent, and a well-behaved cross section is obtained for all Q_T values. As explained in Sec. II, our resummed calculation is accurate to next-to-next-to-leading-logarithmic (NNLL) order. It is applicable for values of diphoton transverse momentum that are less than the diphoton mass, i.e., for $Q_T < Q$. When $Q_T \sim Q$, terms of the form $\ln^n(Q_T/Q)$ become small. A perturbative expansion with a single hard scale is then applicable, and the cross section can be obtained from finite-order perturbation theory.

3

In addition to the initial-state logarithmic singularities, there is a set of important final-state singularities which arise in the matrix elements when at least one photon's momentum is collinear to the momentum of a final-state parton. They are sometimes referred to as 'fragmentation' singularities. At lowest order in α_s, the final-state singularity appears only in the $qg \to \gamma\gamma q$ diagrams, as in Fig. 1 (e). There are various methods used in the literature to deal with the final-state singularity, including the introduction of explicit fragmentation functions $D_\gamma(z)$ for hard photon production, where z is the light-cone fraction of the intermediate parton's momentum carried by the photon. These single-photon "one-fragmentation" and "two-fragmentation" contributions, corresponding to one or both photons produced in independent fragmentation processes, are illustrated by the diagrams in Figs. 1 (f) and (g). In addition, a fragmentation contribution of entirely different nature arises when the $\gamma\gamma$ pair is relatively light and produced from fragmentation of *one* parton, as discussed in Secs. II C 2 and III A 3. A full and consistent treatment of the final-state logarithms beyond lowest order would require a joint resummation of the initial- and final-state logarithmic singularities.

In the work reported here, we are guided by our interest in describing the cross section for *isolated* photons, in which the fragmentation contributions are largely suppressed. A typical isolation condition requires the hadronic activity to be minimal (e.g., comparable to the underlying event) in the immediate neighborhood of each candidate photon. Candidate photons can be rejected by energy deposit nearby in the hadronic calorimeter or the presence of hadronic tracks near the photons. A theory calculation may approximate the experimental isolation by requiring the full energy of the hadronic remnants to be less than a threshold "isolation energy" E_T^{iso} in a cone of size ΔR around each photon. The two photons must be also separated in the plane of the rapidity η and azimuthal angle φ by an amount exceeding the resolution $\Delta R_{\gamma\gamma}$ of the detector. The values of E_T^{iso}, ΔR, and $\Delta R_{\gamma\gamma}$ serve as crude characteristics of the actual measurement. The magnitude of the final-state fragmentation contribution depends on the assumed values of E_T^{iso}, ΔR, and $\Delta R_{\gamma\gamma}$.

An additional complication arises when the fragmentation radiation is assumed to be exactly collinear to the photon's momentum, as implied by the photon fragmentation functions $D_\gamma(z)$. The collinear approximation constrains from below the values of z accessible to $D_\gamma(z)$: $z > z_{min}$. The size of the fragmentation contribution may depend strongly on the values of E_T^{iso} and z_{min} as a consequence of rapid variation of $D_\gamma(z)$ with z.

In our work we treat the final-state singularity using a prescription that reproduces desirable features of the isolated cross sections while bypassing some of the technical difficulties alluded to above. For $Q_T > E_T^{iso}$, we avoid the final-state collinear singularity in the qg scattering channel by applying quasi-experimental isolation. When $Q_T < E_T^{iso}$, we apply an auxiliary regulator which approximates on average the full NLO rate from direct qg and fragmentation cross sections in this Q_T range. Two prescriptions for the auxiliary regulator (subtraction and smooth-cone isolation inside the photon's isolation cone) are considered and lead to similar predictions at the Tevatron and the LHC.

We begin with our notation in Sec. II A, followed by an overview of the procedure for resummation of initial-state multiple parton radiation in Sec. II B. The issue of the final-state fragmentation singularity is discussed in Sec. II C. Our approach is compared with that of the DIPHOX calculation [14], in which explicit fragmentation function contributions are included at NLO, but all-orders resummation is not performed. Our theoretical framework is summarized in Sec. II D.

In Sec. III we compare the predictions of our resummation calculation with Tevatron

data. Resummation is shown to be important for the successful description of physical Q_T distributions, as well as for stable estimates of the effects of experimental acceptance on distributions in the diphoton invariant mass. We compare our results with the DIPHOX calculation [14] and demonstrate that the requirement $Q_T < Q$ further suppresses the effects of the final-state fragmentation contribution, beyond the reduction associated with isolation. Next, we present our predictions for distributions of diphoton pairs produced at the energy of the LHC. Various distributions of the diphoton pairs produced from the decay of a Higgs boson are contrasted with those produced from QCD continuum processes at the LHC, showing that enhanced sensitivity to the signal can be obtained with judicious event selection. Our conclusions are presented in Sec. IV.

II. THEORY OVERVIEW

A. Notation

We consider the scattering process $h_1(P_1) + h_2(P_2) \to \gamma(P_3) + \gamma(P_4) + X$, where h_1 and h_2 are the initial-state hadrons. In terms of the center-of-mass collision energy $\sqrt{S}$, the invariant mass Q, transverse momentum Q_T, and rapidity y of the $\gamma\gamma$ pair, the laboratory frame momenta P_1^μ and P_2^μ of the initial hadrons and $q^\mu \equiv P_3^\mu + P_4^\mu$ of the $\gamma\gamma$ pair are

$$P_1^\mu = \frac{\sqrt{S}}{2}\{1,0,0,1\}; \tag{1}$$

$$P_2^\mu = \frac{\sqrt{S}}{2}\{1,0,0,-1\}; \tag{2}$$

$$q^\mu = \left\{\sqrt{Q^2+Q_T^2}\cosh y, Q_T, 0, \sqrt{Q^2+Q_T^2}\sinh y\right\}. \tag{3}$$

The light-cone momentum fractions for the boosted $2 \to 2$ scattering system are

$$x_{1,2} \equiv \frac{2(P_{2,1} \cdot q)}{S} = \frac{\sqrt{Q^2+Q_T^2}e^{\pm y}}{\sqrt{S}}. \tag{4}$$

Decay of the $\gamma\gamma$ pairs is described in the hadronic Collins-Soper frame [15]. The Collins-Soper frame is a rest frame of the $\gamma\gamma$ pair (with $q^\mu = \{Q,0,0,0\}$ in this frame), chosen so that (a) the momenta $\vec{P}_1$ and $\vec{P}_2$ of the initial hadrons lie in the Oxz plane (with zero azimuthal angle), and (b) the z axis bisects the angle between $\vec{P}_1$ and $-\vec{P}_2$. The photon momenta are antiparallel in the Collins-Soper frame:

$$P_3^\mu = \frac{Q}{2}\{0, \sin\theta_* \cos\varphi_*, \sin\theta_* \sin\varphi_*, \cos\theta_*\}, \tag{5}$$

$$P_4^\mu = \frac{Q}{2}\{0, -\sin\theta_* \cos\varphi_*, -\sin\theta_* \sin\varphi_*, -\cos\theta_*\}, \tag{6}$$

where θ_* and φ_* are the photon's polar and azimuthal angles. In this section, we derive resummed predictions for the fully differential $\gamma\gamma$ cross section $d\sigma/(dQ^2 dy dQ_T^2 d\Omega_*)$, where $d\Omega_* = d\cos\theta_* d\varphi_*$ is a solid angle element around the direction of $\vec{P}_3$ in the Collins-Soper frame defined in Eq. (5). The angles in the Collins-Soper frame are denoted by a "$*$" subscript, in contrast to angles in the lab frame, which do not have such a subscript. The parton momenta and helicities are denoted by lowercase p_i and λ_i, respectively.

5

B. Resummation of the initial-state QCD radiation

For completeness, we present an overview of the finite-order and resummed contributions associated with the direct production of diphotons. At the lowest order in the strong coupling strength α_s, photon pairs are produced with zero transverse momentum Q_T. The Born $q\bar{q} \to \gamma\gamma$ cross section corresponding to Fig. 1 (a) is

$$\frac{d\sigma_{q\bar{q}}}{dQ^2 dy\, dQ_T^2 d\Omega_*}\bigg|_{Born} = \delta(\vec{Q}_T) \sum_{i=u,\bar{u},d,\bar{d},...} \frac{\Sigma_i(\theta_*)}{S} f_{q_i/h_1}(x_1,\mu_F) f_{\bar{q}_i/h_2}(x_2,\mu_F), \tag{7}$$

where $f_{q_i/h}(x,\mu_F)$ denotes the parton distribution function (PDF) for a quark of a flavor i, evaluated at a factorization scale μ_F of order Q. The prefactor

$$\Sigma_i(\theta_*) \equiv \sigma_i^{(0)} \frac{1+\cos^2\theta_*}{1-\cos^2\theta_*}, \tag{8}$$

with

$$\sigma_i^{(0)} \equiv \frac{\alpha^2(Q) e_i^4 \pi}{2N_c Q^2}, \tag{9}$$

is composed of the running electromagnetic coupling strength $\alpha \equiv e^2/4\pi$ evaluated at the scale Q, fractional quark charge $e_i = 2/3$ or $-1/3$, and number of QCD colors $N_c = 3$.

The lowest-order $gg \to \gamma\gamma$ scattering proceeds through an amplitude with a virtual quark loop (a box diagram) shown in Fig. 1 (h). Its cross section takes the form

$$\frac{d\sigma_{gg}}{dQ^2 dy\, dQ_T^2 d\Omega_*}\bigg|_{Born} = \delta(\vec{Q}_T) \frac{\Sigma_g(\theta_*)}{S} f_{g/h_1}(x_1,\mu_F) f_{g/h_2}(x_2,\mu_F), \tag{10}$$

where the prefactor

$$\Sigma_g(\theta_*) \equiv \sigma_g^{(0)} L_g(\theta_*) \tag{11}$$

depends on the polar angle θ_* through a function $L_g(\theta_*)$ presented explicitly in Ref. [3]. The overall normalization coefficient

$$\sigma_g^{(0)} = \frac{\alpha^2(Q)\alpha_s^2(Q)}{32\pi Q^2(N_c^2-1)} \left(\sum_i e_i^2\right)^2 \tag{12}$$

involves the sum of the squared charges e_i^2 of the quarks circulating in the loop.

The NLO direct contributions, represented by Figs. 1 (b)-(e), (i)-(l) and denoted as $P(Q,Q_T,y,\Omega_*)$, are computed in Refs. [3, 4, 5, 7, 8, 9, 10]. The NLO $2 \to 3$ differential cross section grows logarithmically if the final-state parton is soft or collinear to the initial-state quark or gluon, i.e., when Q_T of the $\gamma\gamma$ pair is much smaller than Q. These "initial-state" logarithmic contributions are summed to all orders later in this subsection. The NLO qg cross section also contains a large logarithm when one of the photons is produced from a collinear $\overset{(-)}{q} \to \overset{(-)}{q}\gamma$ splitting in the final state. This "final-state" collinear limit is discussed in Section II C.

6

With contributions from the initial-state soft or collinear radiation included, the NLO cross section is approximated in the small-Q_T asymptotic limit by

$$A_{q\bar{q}}(Q,Q_T,y,\Omega_*) = \sum_{i=u,\bar{u},d,\bar{d},\dots} \frac{\Sigma_i(\theta_*)}{S}\left\{\delta(\vec{Q}_T)F_{i,\delta}(Q,y,\theta_*) + F_{i,+}(Q,y,Q_T)\right\} \tag{13}$$

in the $q\bar{q} + qg$ scattering channel, and by

$$\begin{aligned}A_{gg}(Q,Q_T,y,\Omega_*) &= \frac{1}{S}\Bigg\{\Sigma_g(\theta_*)\left[\delta(\vec{Q}_T)F_{g,\delta}(Q,y,\theta_*) + F_{g,+}(Q,y,Q_T)\right]\\ &\quad + \Sigma'_g(\theta_*,\varphi_*)F'_g(Q,y,Q_T)\Bigg\}\end{aligned} \tag{14}$$

in the $gg+gq_S$ scattering channel. The functions $F_{a,\delta}(Q,y,\theta_*)$ and $F_{a,+}^{(\prime)}(Q,y,Q_T)$ for relevant parton flavors a are listed in Appendix B. They include 'plus function' contributions of the type $\left[Q_T^{-2}\ln^p\left(Q^2/Q_T^2\right)\right]_+$ with $p \geq 0$, universal functions describing soft and collinear scattering, and process-dependent corrections from NLO virtual diagrams.

The $q\bar{q} + qg$ asymptotic cross section $A_{q\bar{q}}(Q,Q_T,y,\Omega_*)$ is proportional to the angular function $\Sigma_i(\theta_*)$, the same as in the Born $q\bar{q} \to \gamma\gamma$ cross section, cf. Eq. (7). Similarly, the $gg+gq_S$ asymptotic cross section $A_{gg}(Q,Q_T,y,\Omega_*)$ includes a term proportional to the Born angular function $\Sigma_g(\theta_*)$. In addition, $A_{gg}(Q,Q_T,y,\Omega_*)$ contains another term proportional to $\Sigma'_g(\theta_*,\varphi_*) \equiv L'_g(\theta_*)\cos 2\varphi_*$, where $L'_g(\theta_*)$ is derived in Ref. [3]. This term arises due to the interference of Born amplitudes with incoming gluons of opposite polarizations and affects the azimuthal angle (φ_*) distribution of the photons in the Collins-Soper frame [3].

The small-Q_T representations in Eqs. (13) and (14) can be used to compute fixed-order particle distributions in the phase-space slicing method. In this method, we choose a small Q_T value Q_T^{sep} in the range of validity of Eqs. (13) and (14). If the actual Q_T in the computation exceeds Q_T^{sep}, we calculate the differential cross section using the full $2 \to 3$ matrix element. When Q_T is smaller than Q_T^{sep}, we calculate the event rate using the small-Q_T asymptotic approximation $A(Q,Q_T,y,\Omega_*)$ and $2 \to 2$ phase space. Hence, the lowest bin of the Q_T distribution is approximated in the NLO prediction by its *average* value in the interval $0 \leq Q_T \leq Q_T^{sep}$, computed by integration of the asymptotic approximations.

The phase-space slicing procedure is sufficient for predictions of observables inclusive in Q_T, but not of the shape of $d\sigma/dQ_T$ distributions. The latter goal is met by all-orders summation of singular asymptotic contributions with the help of the Collins-Soper-Sterman (CSS) method [11, 16, 17]. The small-Q_T resummed cross section is denoted as $W(Q,Q_T,y,\Omega_*)$ and given by a two-dimensional Fourier transform of a function $\widetilde{W}(Q,b,y,\Omega_*)$ that depends on the impact parameter $\vec{b}$:

$$\begin{aligned}W(Q,Q_T,y,\Omega_*) &= \int \frac{d\vec{b}}{(2\pi)^2}e^{i\vec{Q}_T\cdot\vec{b}}\widetilde{W}(Q,b,y,\Omega_*)\\ &\equiv \int \frac{d\vec{b}}{(2\pi)^2}e^{i\vec{Q}_T\cdot\vec{b}}\widetilde{W}_{pert}(Q,b_*,y,\Omega_*)e^{-\mathcal{F}_{NP}(Q,b)}.\end{aligned} \tag{15}$$

In this equation, $\widetilde{W}(Q,b,y,\Omega_*)$ is written as a product of the perturbative part $\widetilde{W}_{pert}(Q,b_*,y,\Omega_*)$ and the nonperturbative exponent $\exp\left(-\mathcal{F}_{NP}(Q,b)\right)$, which describe the

dynamics at small ($b \lesssim 1 \text{ GeV}^{-1}$) and large ($b \gtrsim 1 \text{ GeV}^{-1}$) impact parameters, respectively. The purpose of the variable b_* is reviewed below.

If Q is large, the perturbative form factor $\widetilde{W}_{pert}$ dominates the integral in Eq. (15). It is computed at small b as

$$
\begin{aligned}
\widetilde{W}_{pert}(Q,b,y,\theta_*) = &\sum_a \frac{\Sigma_a(\theta_*)}{S} h_a^2(Q,\theta_*) e^{-\mathcal{S}_a(Q,b)} \\
&\times \left[\mathcal{C}_{a/a_1} \otimes f_{a_1/h_1}\right](x_1,b;\mu) \left[\mathcal{C}_{\bar{a}/a_2} \otimes f_{a_2/h_2}\right](x_2,b;\mu).
\end{aligned}
\tag{16}
$$

The "hard-vertex" function $\Sigma_a(\theta_*)h_a^2(Q,\theta_*)$ is the normalized cross section for the Born scattering $a\bar{a} \rightarrow \gamma\gamma$, with $a = u, \bar{u}, d, \bar{d}, ...$ in $q\bar{q} \rightarrow \gamma\gamma$, and $a = \bar{a} = g$ in $gg \rightarrow \gamma\gamma$. The Sudakov exponent

$$
\mathcal{S}_a(Q,b) = \int_{C_1^2/b^2}^{C_2^2 Q^2} \frac{d\bar{\mu}^2}{\bar{\mu}^2} \left[\mathcal{A}_a\left(C_1,\bar{\mu}\right) \ln\left(\frac{C_2^2 Q^2}{\bar{\mu}^2}\right) + \mathcal{B}_a\left(C_1,C_2,\bar{\mu}\right)\right]
\tag{17}
$$

is an integral of two functions $\mathcal{A}_a\left(C_1,\bar{\mu}\right)$ and $\mathcal{B}_a\left(C_1,C_2,\bar{\mu}\right)$ between momentum scales C_1/b and $C_2 Q$, and C_1 and C_2 are constants of order $c_0 \equiv 2e^{-\gamma_E} = 1.123...$ and 1, respectively. The symbol $\left[\mathcal{C}_{a/a_1} \otimes f_{a_1/h}\right](x,b;\mu)$ stands for a convolution of the k_T-integrated PDF $f_{a_1/h}(x,\mu)$ and Wilson coefficient function $\mathcal{C}_{a/a_1}(x,b;C_1/C_2,\mu)$, evaluated at a factorization scale μ and summed over intermediate parton flavors a_1:

$$
\left[\mathcal{C}_{a/a_1} \otimes f_{a_1/h}\right](x,b;\mu) \equiv \sum_{a_1} \left[\int_x^1 \frac{d\xi}{\xi} \mathcal{C}_{a/a_1}\left(\frac{x}{\xi},b;\frac{C_1}{C_2},\mu\right) f_{a_1/h}(\xi,\mu)\right].
\tag{18}
$$

We compute the functions h_a, $\mathcal{A}_a$, $\mathcal{B}_a$ and $\mathcal{C}_{a/a_1}$ up to orders α_s, α_s^3, α_s^2, and α_s, respectively, corresponding to the NNLL accuracy of resummation. The perturbative coefficients at these orders in α_s are listed in Appendix A.

The subleading contribution from the nonperturbative region $b \gtrsim 1 \text{ GeV}^{-1}$ is included in our calculation using a revised "b_*" model [18], which provides excellent agreement with p_T-dependent data on Drell-Yan pair and Z boson production. In this model, the perturbative form factor $\widetilde{W}_{pert}(Q,b_*,y,\Omega_*)$ in Eq. (15) is evaluated as a function of $b_* \equiv b/(1+b^2/b_{max}^2)^{1/2}$, with $b_{max} = 1.5 \text{ GeV}^{-1}$. The factorization scale μ in $[\mathcal{C} \otimes f]$ is set equal to $c_0\sqrt{b^{-2} + Q_{ini}^2}$, where Q_{ini} is the initial scale of order 1 GeV in the parameterization employed for $f_{a/h}(x,\mu)$, for instance, 1.3 GeV for the CTEQ6 PDFs [19]. We have $\widetilde{W}_{pert}(b_*) = \widetilde{W}_{pert}(b)$ at $b^2 \ll b_{max}^2$, and $\widetilde{W}_{pert}(b_*) = \widetilde{W}_{pert}(b_{max})$ at $b^2 \gg b_{max}^2$. Hence, this ansatz preserves the exact form of the perturbative form factor $\widetilde{W}_{pert}(Q,b,y,\Omega_*)$ in the perturbative region of small b, while also incorporating the leading nonperturbative contributions (described by a phenomenological function $\mathcal{F}_{NP}(Q,b)$) at large b.

The form of $\mathcal{F}_{NP}(Q,b)$ found in the global p_T fit in Ref. [18] suggests approximate independence of $\mathcal{F}_{NP}(Q,b)$ from the type of $q\bar{q}$ scattering process. It is used here to describe the nonperturbative terms in the leading $q\bar{q} \rightarrow \gamma\gamma$ channel. We neglect possible corrections to the nonperturbative contributions arising from the final-state soft radiation in the qg channel and additional $\sqrt{S}$ dependence affecting Drell-Yan-like processes at $x \lesssim 10^{-2}$ [20], as these exceed the accuracy of the present measurements at the Tevatron. The experimentally unknown $\mathcal{F}_{NP}(Q,b)$ in the gg channel is approximated by $\mathcal{F}_{NP}(Q,b)$ for the $q\bar{q}$ channel,

multiplied by the ratio $C_A/C_F = 9/4$. This choice is motivated by the fact that the leading Sudakov color factors $\mathcal{A}_a^{(k)}$ in the gg and $q\bar{q}$ channels are proportional to $C_A = 3$ and $C_F = 4/3$, respectively. The uncertainties in the $\gamma\gamma$ cross sections associated with $\mathcal{F}_{NP}(Q, b)$ are investigated numerically in Ref. [3].

In the region $Q_T \sim Q$, collinear QCD factorization at a finite fixed order in α_s is applicable. In order to include non-singular contributions important in this region, we add to $W(Q, Q_T, y, \Omega_*)$ the regular piece $Y(Q, Q_T, y, \Omega_*)$, defined as the difference between the NLO cross section $P(Q, Q_T, y, \Omega_*)$ and its small-Q_T asymptotic approximation $A(Q, Q_T, y, \Omega_*)$:

$$
\begin{aligned}
\frac{d\sigma(h_1 h_2 \to \gamma\gamma)}{dQ\, dQ_T^2\, dy\, d\Omega_*} &= W(Q, Q_T, y, \Omega_*) + P(Q, Q_T, y, \Omega_*) - A(Q, Q_T, y, \Omega_*) \\
&\equiv W(Q, Q_T, y, \Omega_*) + Y(Q, Q_T, y, \Omega_*).
\end{aligned}
\tag{19}
$$

At small Q_T, subtraction of $A(Q, Q_T, y, \Omega_*)$ in Eq. (19) cancels large initial-state radiative corrections in $P(Q, Q_T, y, \Omega_*)$, which are incorporated in their resummed form within $W(Q, Q_T, y, \Omega_*)$. At Q_T comparable to Q, $A(Q, Q_T, y, \Omega_*)$ cancels the leading terms in $W(Q, Q_T, y, \Omega_*)$, but higher-order contributions remain from the infinite tower of logarithmic terms that are resummed in W. In this situation the $W + Y$ cross section drops below the finite-order result $P(Q, Q_T, y, \Omega_*)$ at some value of Q_T (referred to as the *crossing point*) in both the $q\bar{q} + qg$ and $gg + gq_S$ channels, for each Q and y. We use the $W + Y$ cross section as our final prediction at Q_T values below the crossing point, and the NLO cross section P at Q_T values above the crossing point.

A few comments are in order about our resummation calculation. The hard-vertex contribution $\Sigma_a(\theta_*) h_a^2(Q, \theta_*)$ and the functions $\mathcal{B}_a(C_1, C_2, \bar{\mu})$ and $\mathcal{C}_{a/a_1}(x, b; C/C_2, \mu)$ can be varied in a mutually compensating way while preserving the same value of the form factor W up to higher-order corrections in α_s. This ambiguity, or dependence on the chosen "resummation scheme" [21] within the CSS formalism, can be employed to explore the sensitivity of theoretical predictions to further next-to-next-to-next-to-leading logarithmic (NNNLL) effects that are not accounted for explicitly.

The perturbative coefficients in Appendix A are presented in the CSS resummation scheme [11], our default choice in numerical calculations, and in an alternative scheme by Catani, de Florian and Grazzini (CFG) [21]. In the original CSS resummation scheme, the $\mathcal{B}$ and $\mathcal{C}$ functions contain the finite virtual NLO corrections to the $2 \to 2$ scattering process, whereas in the CFG scheme the universal $\mathcal{B}$ and $\mathcal{C}$ depend only on the type of incident partons, and the process-dependent virtual correction is included in the function h_a. The difference between the CSS and CFG schemes is numerically small in $\gamma\gamma$ production at both the Tevatron and the LHC [3].

In the $gg + gq_S$ scattering channel, the unpolarized resummed cross section includes an additional contribution from elements of k_T-dependent PDF spin matrices with opposite helicities of outgoing gluons [3]. The NLO expansion of this spin-flip resummed cross section generates the term proportional to $\Sigma_g'(\theta_*, \varphi_*) \propto \cos 2\varphi_*$ in the small-Q_T asymptotic cross section, cf. Eq. (14). Although the logarithmic spin-flip contribution must be resummed in principle to all orders to predict the φ_* dependence in the $gg + gq_S$ channel, it is neglected in the present work in view of its small effect on the full $\gamma\gamma$ cross section.

When integrated over Q_T from 0 to scales of order Q, the resummed cross section becomes approximately equal to the finite-order (NLO) cross section, augmented typically by a few-percent correction from integrated higher-order terms logarithmic in Q_T. Inclusive

observables that allow such integration (e.g., the large-Q region of the $\gamma\gamma$ invariant mass distribution) are approximated well both by the resummed and NLO calculations. However, the experimental acceptance constrains the range of the integration over Q_T in parts of phase space and may break delicate cancellations between integrable singularities present in the finite-order differential distribution. In this situation (e.g., in the vicinity of the kinematic cutoff in $d\sigma/dQ$ discussed in Sec. III) the NLO cross section becomes unstable, while the resummed cross section (free of discontinuities) continues to depend smoothly on kinematic constraints. We see that the resummation is essential not only for the prediction of physical Q_T distributions in $\gamma\gamma$ production, but also for credible estimates of the effects of experimental acceptance on distributions in the diphoton invariant mass and other variables.

C. Final-state photon fragmentation

1. Single-photon fragmentation

In addition to the QCD singularities associated with initial-state radiation [described by the asymptotic terms in Eqs. (13) and (14)], other singularities arise in the $\mathcal{O}(\alpha_s)$ process $q(p_1) + g(p_2) \to \gamma(p_3) + \gamma(p_4) + q(p_5)$ [Fig. 1 (e)] when a photon is collinear to the final-state quark. In this limit, the $qg \to q\gamma\gamma$ squared matrix element grows as $1/s_{\gamma 5}$, when $s_{\gamma 5} \to 0$, where $s_{\gamma 5}$ is the squared invariant mass of the collinear γq pair. In this limit, the squared matrix element factors as

$$|\mathcal{M}(qg \to q\gamma\gamma)|^2 \approx \frac{2e^2 e_i^2}{s_{\gamma 5}} P_{\gamma \leftarrow q}(z) |\mathcal{M}(qg \to q\gamma)|^2 \tag{20}$$

into the product of the squared matrix element $|\mathcal{M}(qg \to q\gamma)|^2$ for the production of a photon and an intermediate quark, and a splitting function $P_{\gamma \leftarrow q}(z) = (1 + (1-z)^2)/z$ for fragmentation of the intermediate quark into a collinear γq pair. In Eq. (20) z is the light-cone fraction of the intermediate quark's momentum carried by the fragmentation photon, and ee_i is the charge of the intermediate quark. When the photon-quark separation $\Delta r = \sqrt{(\eta_5 - \eta_\gamma)^2 + (\varphi_5 - \varphi_\gamma)^2}$ in the plane of pseudorapidity $\eta = -\log(\tan(\theta/2))$ and azimuthal angle φ in the lab frame is small, as in the collinear limit, $s_{\gamma 5} \approx E_{T\gamma} E_{T5} \Delta r^2$, where $E_{T\gamma}$ and E_{T5} are the transverse energies of the photon and quark, with $E_T \equiv E \sin\theta$. Note that $E_{T5} = Q_T$ at the order in α_s at which we are working. Therefore, contributions from the final-state collinear, or fragmentation, region are most pronounced at small Δr and relatively small Q_T.[1]

A fully consistent treatment of the initial- and final-state singularities would require a joint initial- and final-state resummation. In the approaches taken to date, the fragmentation singularity may be subtracted from the direct cross section and replaced by a single-photon "one-fragmentation" contribution $q + g \to (q \xrightarrow{frag} \gamma) + \gamma$, where "$(q \xrightarrow{frag} \gamma)$" denotes collinear production of one hard photon from a quark, described by a function $D_\gamma(z, \mu)$ at a light-cone momentum fraction z and factorization scale μ. Single-photon "two-fragmentation"

---

[1] In the soft, or $E_5 \to 0$, limit, the final-state collinear contribution is suppressed, reflecting the absence of the soft singularity in the $qg \to q\gamma\gamma$ cross section.

contributions arise in processes like $g + g \rightarrow (q \xrightarrow{frag} \gamma) + (\bar{q} \xrightarrow{frag} \gamma)$ and involve convolutions with two functions $D_\gamma(z, \mu)$ (one per photon). The lowest-order Feynman diagrams for the one- and two-fragmentation contributions are shown in Figs. 1(f) and 1(g), respectively. Parameterizations must be adopted for the nonperturbative functions $D_\gamma(z, \mu)$ at an initial scale $\mu = \mu_0$. This is the approach followed in the DIPHOX calculation [14], in which the sum of real and virtual NLO corrections to direct and single-γ fragmentation cross sections is included. When explicit fragmentation function contributions are included, the inclusive rate is increased by higher-order contributions from photon production within hadronic jets. However, much of the enhancement is suppressed by isolation constraints imposed on the inclusive photon cross sections before the comparison with data. Nevertheless, fragmentation contributions surviving isolation may be moderately important in parts of phase space.

An infrared-safe procedure can be formulated to apply isolation cuts at each order of α_s [22, 23, 24]. This procedure encounters difficulties in reproducing the effects of isolation on fragmentation contributions, because theoretical models reflect only basic features of the experimental isolation and may introduce new logarithmic singularities near the edges of the isolation cones.

As mentioned in the Introduction, the magnitude of the fragmentation contribution depends on the values of isolation parameters E_T^{iso}, ΔR, and $\Delta R_{\gamma\gamma}$, modeled only approximately in a theoretical calculation. The collinear approximation constrains from below the values of z accessible to $D_\gamma(z, \mu)$: $z > z_{min} \equiv (1 + E_{T5}^{iso}/E_{T\gamma})^{-1}$. If $D_\gamma(z, \mu)$ varies rapidly with z, the fragmentation cross section is particularly sensitive to the assumed values of E_T^{iso} and z_{min}. For instance, if $D_\gamma(z, \mu) \sim 1/z$, the fragmentation cross section is roughly proportional to E_T^{iso} under a typical condition $E_T^{iso}/E_{T\gamma} \ll 1$. Such nearly linear dependence on E_T^{iso} of the fragmentation cross section $d\sigma/dQ_T$ is indeed observed in the DIPHOX calculation, as reviewed in Sec. III. In reality, some spread of the parton radiation in the direction transverse to the photon's motion is expected. The treatment of kinematics in parton showering programs like PYTHIA results in somewhat different dependence on z [12] compared to the collinear approximation, hence in a different magnitude of the fragmentation cross section.

In this work we adopt a procedure that reproduces desirable features of the isolated cross sections, while bypassing some of the difficulties summarized above. To simulate experimental isolation, we reject an event if (a) the separation Δr between the final-state parton and one of the photons is less than ΔR, and (b) E_{T5} of the parton is larger than E_T^{iso}. This condition is applied to the NLO cross section $P(Q, Q_T, y, \Omega_*)$, but not to $W(Q, Q_T, y, \Omega_*)$ and $A(Q, Q_T, y, \theta_*)$, as these correspond to initial-state QCD radiation and are free of the final-state collinear singularity.

This quasi-experimental isolation excludes the singular final-state direct contributions at $E_{T5} > E_T^{iso}$ and $\Delta r < \Delta R$ (or $s_{\gamma5} < E_{T\gamma} E_{T5} \Delta R^2$). It is effective for $Q_T > E_T^{iso}$, but the collinear direct contributions survive when $Q_T < E_T^{iso}$. The integrated (but not the differential) fragmentation rate in the region $Q_T < E_T^{iso}$ may be estimated from a calculation with explicit fragmentation functions. In our approach, we do not introduce fragmentation functions, but we apply an auxiliary regulator to the direct qg cross section at $Q_T < E_T^{iso}$ and $\Delta r < \Delta R$. In our numerical study we find that this prescription preserves a continuous differential distribution except for a small finite discontinuity at $Q_T = E_T^{iso}$. It approximately reproduces the integrated qg rate obtained in the DIPHOX calculation at small Q_T, for the nominal E_T^{iso}.
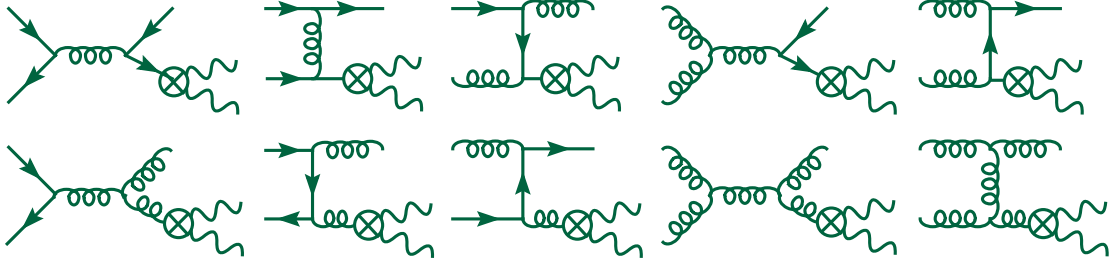
Figure 2: Lowest-order Feynman diagrams describing fragmentation of the final-state partons into photon pairs with relatively small mass Q.

Two forms of the auxiliary regulator are considered below, based on subtraction of the leading collinear contribution and smooth-cone isolation [25]. In the first case, we subtract the leading part Eq. (20) of the direct qg matrix element when $E_{T5} < E_T^{iso}$ and $\Delta r < \Delta R$. We take $z = 1 - p_s \cdot p_5/(p_s \cdot p_f + p_s \cdot p_5 + p_f \cdot p_5)$, where p_f^μ, p_5^μ, and p_s^μ are the four-momenta of the fragmentation photon, fragmentation quark, and spectator photon, respectively [26]. This prescription is used in most of the numerical results in this paper.

In the second case, we suppress fragmentation contributions at $\Delta r < \Delta R$ and $E_{T5} < E_T^{iso}$ by rejecting events in the ΔR cone that satisfy $E_{T5} < \chi(\Delta r)$, where $\chi(\Delta r)$ is a smooth function satisfying $\chi(0) = 0$, $\chi(\Delta R) = E_T^{iso}$. This "smooth-cone isolation" [25] transforms the fragmentation singularity associated with $D_\gamma(z, \mu)$ into an integrable singularity, which depends on the assumed functional form of $\chi(\Delta r)$. The cross section for direct contributions is rendered finite by this prescription without explicit introduction of fragmentation functions $D_\gamma(z, \mu)$. For our smooth function, we choose $\chi(\Delta r) = E_T^{iso}(1 - \cos \Delta r)^2/(1 - \cos \Delta R)^2$, which differs from the specific form considered in Ref. [25], but still satisfies the condition $\chi(0) = 0$. Our earlier results in Ref. [2] are computed with this prescription. Here we employ it only in a few instances for comparison with the subtraction method and obtain similar results.

Differences between the two prescriptions can be used to quantify sensitivity of the predictions to the treatment of the $Q_T < E_T^{iso}$ and $\Delta r < \Delta R$ region. The two prescriptions yield identical predictions outside of this restricted region, notably at $Q_T > E_T^{iso}$, where our NLO perturbative expression $P(Q, Q_T, y, \Omega_*)$ in the $q\bar{q} + qg$ channel is controlled only by quasi-experimental isolation and coincides with the corresponding direct cross section in DIPHOX. The default subtraction prescription predicts a vanishing $d\sigma/dQ_T$ in the extreme $Q_T \to 0$ limit, while the smooth-cone prescription has an integrable singularity in this limit, avoided by an explicit small-Q_T cutoff in the calculation of our Y-piece. Both prescriptions are free of the logarithmic singularity at $Q_T = E_T^{iso}$ arising in the fixed-order (DIPHOX) calculation.

2. Low-Q diphoton fragmentation

Another class of large radiative corrections arises when the $\gamma\gamma$ invariant mass Q is smaller than the $\gamma\gamma$ transverse momentum Q_T. In this case, one final-state quark or gluon fragments into a low-mass $\gamma\gamma$ pair, e.g. as $q + g \to (q \xrightarrow{frag} \gamma\gamma) + g$. The lowest-order contributions of this kind are shown in Fig. 2. The process is described by a $\gamma\gamma$-fragmentation function $D_{\gamma\gamma}(z_1, z_2, \mu)$, different from the single-photon fragmentation function $D_\gamma(z, \mu)$. This

new "two-photons from one-fragmentation" contribution is not included yet in existing calculations, even though similar fragmentation mechanisms have been studied in large-Q_T Drell-Yan pair production [27, 28]. The importance of low-Q $\gamma\gamma$-fragmentation may be elevated in some kinematic regions for typical experimental cuts. They can be removed by adjustments in the experimental cuts, as discussed in Sec. III.

D. Summary of the calculation

We conclude this section by summarizing the main features of our calculation. Full direct NLO cross sections, represented by the graphs (a)-(e), (h)-(l) in Fig. 1, are computed, and their initial-state soft/collinear logarithmic singularities are resummed at small Q_T in both the $q\bar{q}+qg$ and $gg+gq_S$ channels. The perturbative Sudakov functions $\mathcal{A}$ and $\mathcal{B}$ and Wilson coefficient functions $\mathcal{C}$ in the resummed cross section W are computed up to orders α_s^3, α_s^2, and α_s, respectively, corresponding to resummation at NNLL accuracy.

Our resummation calculation requires an integration over all values of impact parameter b, including the nonperturbative region of large b. In our default calculation of the resummed cross section, we adopt the nonperturbative functions introduced in Ref. [18]. We consider two resummation schemes, the traditional scheme introduced in the CSS paper as well as an alternative scheme [21]. The comparison allows us to estimate the magnitude of yet higher-order corrections that are not included. The size of these effects is different in the $q\bar{q}+qg$ and $gg+gq_S$ channels but not particularly significant in either [3].

The final-state collinear singularity in the qg scattering channel is avoided by applying quasi-experimental isolation when $Q_T > E_T^{iso}$ and an auxiliary regulator when $Q_T < E_T^{iso}$ to approximate on average the full NLO rate from direct qg and fragmentation cross sections in this Q_T range. Two prescriptions for the auxiliary regulator (subtraction and smooth isolation inside the photon's isolation cone) are considered and lead to similar predictions at the Tevatron and LHC.

The singular logarithmic contributions associated with initial-state radiation are subtracted from the NLO cross section P to form a regular piece Y, which is added to the small-Q_T resummed cross section W to predict the production rate for small and intermediate values of Q_T. In the $gg+gq_S$ channel, we also subtract from P a new singular spin-flip contribution that affects azimuthal angle (φ_*) dependence in the Collins-Soper reference frame. We switch our prediction to the fixed-order perturbative result P at the point in Q_T where the cross section $W+Y$ drops below P. This crossing point is located at Q_T of order Q in both $q\bar{q}+qg$ and $gg+gq_S$ channels.

III. COMPARISONS WITH DATA AND PREDICTIONS

Our calculation of the differential cross section $d\sigma/(dQdQ_Tdyd\Omega_*)$ is especially pertinent for the transverse momentum Q_T distribution in the region $Q_T \lesssim Q$, for fixed values of diphoton mass Q (cf. Section III A 1). It would be best to compare our *multiple* differential distribution with experiment, but published collider data tend to be presented in the form of singly differential distributions in Q, Q_T, and $\Delta\varphi \equiv \varphi_3 - \varphi_4$ in the lab frame, after integration over the other independent kinematic variables. We follow suit in order to make comparisons with Tevatron collider data, but we recommend that more differential studies

13

be made, and we comment on the features that can be explored. We show results at the energy of the Tevatron collider and then make predictions for the Large Hadron Collider.

The analytical results of Sec. II are implemented in our computer code. As a first step, resummed and NLO $\gamma\gamma$ cross sections are computed on a grid of discrete values of Q, Q_T, and y by using the resummation program LEGACY described in Refs. [29, 30]. At the second stage, matching of the resummed and NLO cross sections is performed, and fully differential cross sections are evaluated by Monte-Carlo integration of the matched grids in the latest version of the program RESBOS [31, 32]. The calculation is done for $N_f = 5$ active quark flavors and the following values of the electroweak and strong interaction parameters [33]:

$$G_F = 1.16639 \times 10^{-5} \text{ GeV}^{-2}, \quad m_Z = 91.1882 \text{ GeV}, \tag{21}$$
$$\alpha(m_Z) = 1/128.937, \quad \alpha_s(m_Z) = 0.1187. \tag{22}$$

The following choices of the factorization constants are used: $C_1 = C_3 = 2e^{-\gamma_E} \approx 1.123...$, and $C_2 = C_4 = 1$. The choice $C_4 = 1$ implies that we equate the renormalization and factorization scales to the invariant mass of the photon pair, $\mu_R = \mu_F = Q$, in the fixed-order and asymptotic contributions $P(Q, Q_T, y, \Omega_*)$ and $A(Q, Q_T, y, \Omega_*)$. We use two-loop expressions for the running electromagnetic and strong couplings $\alpha(\mu)$ and $\alpha_S(\mu)$, as well as the NLO parton distribution function set CTEQ6M [19] with $Q_{ini} = 1.3$ GeV. For calculations with explicit final-state fragmentation functions included, we use set 1 of the NLO photon fragmentation functions from Ref. [34].

A. Results for Run 2 at the Tevatron

1. Kinematic constraints

In this section, we present our results for the Tevatron $p\bar{p}$ collider operating at $\sqrt{S} = 1.96$ TeV. In order to compare with the data from the Collider Detector at Fermilab (CDF) collaboration [1], we make the same restrictions on the final-state photons as those used in the experimental measurement (unless stated otherwise):

transverse momentum $p_T^\gamma > p_{T\,min}^\gamma = 14$ (13) GeV for the harder (softer) photon, (23)
and rapidity $|y^\gamma| < 0.9$ for each photon. (24)

We impose isolation conditions described in Section II C, assuming the nominal isolation energy $E_T^{iso} = 1$ GeV specified in the CDF publication, along with $\Delta R = 0.4$, and $\Delta R_{\gamma\gamma} = 0.3$.

We also show predictions for the constraints that approximate event selection conditions used by the Fermilab DØ Collaboration [35]: $p_T^\gamma > p_{T\,min}^\gamma = 21$ (20) GeV for the harder (softer) photon, $|y^\gamma| < 1.1$, and $E_T^{iso}/E_T^\gamma = 0.07$ for each photon, for the same ΔR and $\Delta R_{\gamma\gamma}$ values as in the CDF case.

A scatter plot of event distributions from our theoretical simulation for CDF kinematic cuts and arbitrary luminosity is shown in Fig. 3. The events are plotted versus the invariant mass Q, transverse momentum Q_T, rapidity separation $|\Delta y| \equiv |y_{hard} - y_{soft}|$, and azimuthal separation $\Delta\varphi \equiv |\varphi_{hard} - \varphi_{soft}|$ (with $0 \leq \Delta\varphi \leq \pi$) between the harder and softer photon in the lab frame, as well as the cosine of the polar angle θ_* in the Collins-Soper frame. It can be seen from the figure that $\Delta\varphi$ is correlated with the difference $Q_T - Q$. Events with
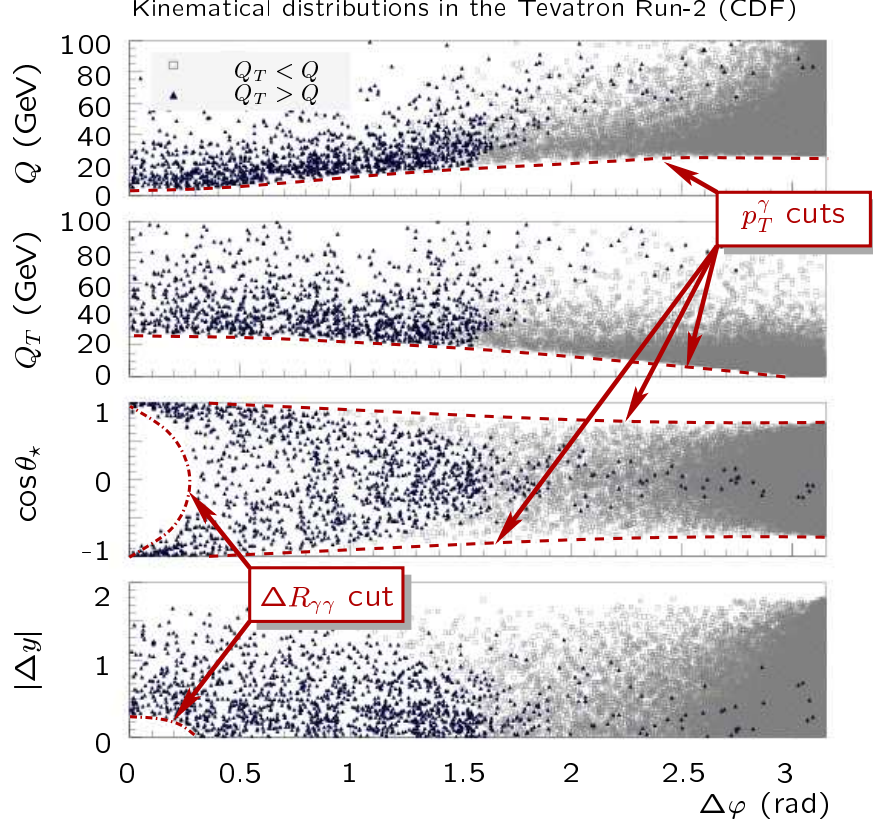
Figure 3: The diphoton event distribution from the theoretical simulation for $\sqrt{S} = 1.96\,\text{GeV}$, with the selection criteria imposed in the CDF measurement, as a function of the various kinematic variables described in the text, shown for $Q_T < Q$ and $Q_T > Q$ separately.

$Q_T < Q$ ($Q_T > Q$) tend to populate regions with $\Delta\varphi > \pi/2$ ($\Delta\varphi < \pi/2$). The extreme case $Q_T = 0$ relevant to the Born approximation corresponds to $\Delta\varphi = \pi$.

The p_T^γ cuts suppress the mass region $Q \lesssim 2\sqrt{p_{Tmin}^{\gamma3} p_{Tmin}^{\gamma4}} \approx 27$ GeV at $\Delta\varphi \approx \pi$ and $Q_T \lesssim 25$ GeV at $\Delta\varphi \approx 0$, leading to the appearance of a kinematic cutoff in the invariant mass distribution and a "shoulder" in the transverse momentum distribution, as shown in later sections. Our theoretical framework is applicable in the region $Q_T \lesssim Q$ (large $\Delta\varphi$), where the dominant fraction of events occurs. The appearance of singularities in the NLO calculation at $Q_T \to 0$ and the fact that there are two different hard scales, Q_T and Q, relevant for the event distributions in the low-Q_T region require that we address and resum large logarithmic terms of the form $\log(Q/Q_T)$. Different and interesting physics becomes important in the complementary region $Q_T > Q$ (small $\Delta\varphi$), a topic we address in Sec. III A 3.

2. Tevatron cross sections

We compare our resummed and finite-order predictions for the invariant mass (Q) distribution of photon pairs, shown in Fig. 4 as solid and dashed lines, respectively. The finite-order cross section is evaluated at $O(\alpha_s)$ accuracy in the $q\bar{q} + qg$ channel and at $O(\alpha_s^3)$ accuracy in the $gg + gq_S$ channel. These finite-order calculations are performed with the
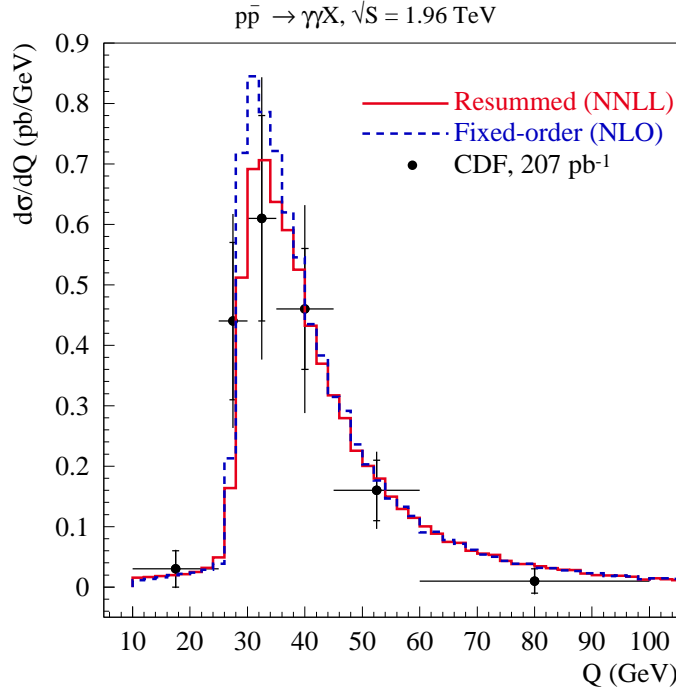
15

Figure 4: Invariant mass distributions of photon pairs in $p\bar{p} \to \gamma\gamma X$ at $\sqrt{S} = 1.96$ TeV with QCD contributions calculated in the soft–gluon resummation formalism (red solid) and at NLO (blue dashed). The calculations include the cuts used by the CDF collaboration whose data are shown [1].

phase-space slicing method described in Sec. II B. When integrated over all Q_T, as in the $d\sigma/dQ$ distribution at large Q, the resummed logarithmic terms from higher orders in α_s produce a relatively small NNLO correction, such that the resummed and finite-order mass distributions in Fig. 4 are close to one another in normalization and shape. Both distributions also agree with the CDF data in this Q range within experimental uncertainties.

The shape of $d\sigma/dQ$ at small Q is affected by the cuts in Eq. (23) on the transverse momenta p_T^γ of the two photons. In addition to being responsible for the characteristic cutoff at $Q \approx 27$ GeV explained in the previous subsection, the cuts on the individual transverse momenta p_T^γ also introduce a dependence of the invariant mass distribution on the shape of the Q_T spectrum of the $\gamma\gamma$ pairs. Because of this correlation between the Q and Q_T distributions, the discontinuities in $d\sigma/dQ_T$ as $Q_T \to 0$, when computed at finite order, make finite-order predictions for $d\sigma/dQ$ somewhat unstable.

The finite-order expectation for the transverse momentum distribution $d\sigma/dQ_T$ (i.e., the integral of $P(Q, Q_T, y, \Omega_*)$ over Q, y, and Ω_*, or P for brevity) is shown as a dashed curve in Fig. 5(a). It exhibits an integrable singularity in the small-Q_T limit. Terms with inverse power and logarithmic dependence on Q_T, associated with initial-state radiation as $Q_T \to 0$, are extracted from P and form the asymptotic contribution, denoted as A (dotted curve). In the figure, both P and A are truncated at a small value of Q_T, that is, not drawn all the way to $Q_T = 0$. The curves for P and A are close at small values of Q_T, signaling that the initial-state logarithmic singularities dominate the NLO distribution. The difference Y
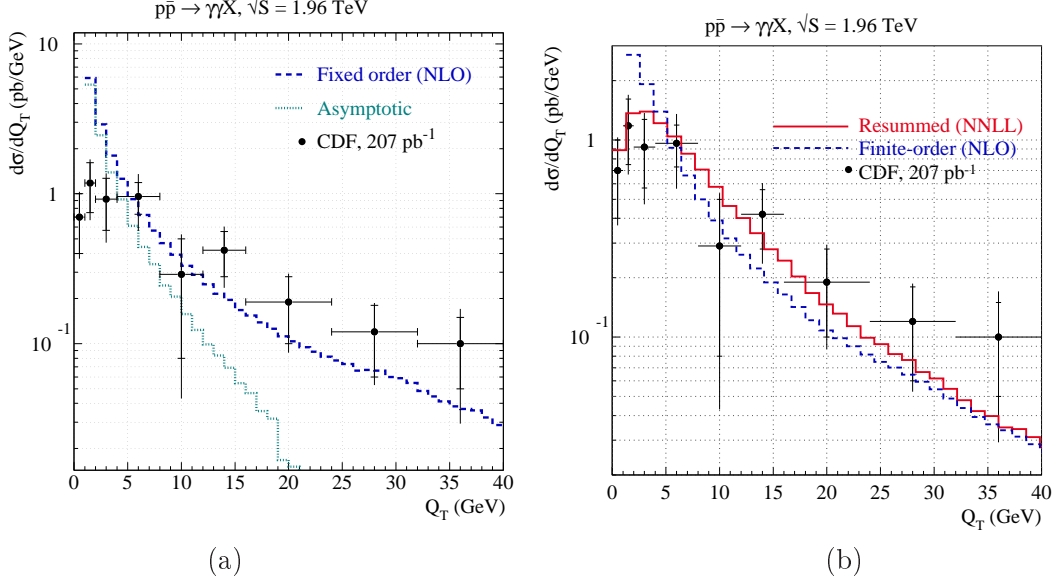
Figure 5: Transverse momentum distributions in $p\bar{p} \to \gamma\gamma X$ at $\sqrt{S} = 1.96$ TeV along with the CDF data: (a) the fixed-order prediction P (dashes) and its asymptotic approximation A (dots); (b) the full resummed cross section (solid), obtained by matching the resummed $W + Y$ to the fixed-order prediction P (dashed, same as in (a)) at large Q_T.

between the P and A distributions includes the finite regular terms not included in A and logarithmic terms from the final-state fragmentation singularities, with the latter subtracted when $Q_T < E_T^{iso}$, as described in Sec. II C. The data clearly disfavor the fixed-order prediction in the region of low Q_T.

Figure 5(b) features the resummed $W + Y$ contribution (solid curve). Resummation of the initial-state logarithmic terms renders W finite in the region of small Q_T. The sum of W and Y includes the resummed initial-state singular contributions plus the remaining relevant terms in P. Since P provides a reliable fixed-order estimate at large Q_T, we present our final resummed prediction by switching from $W + Y$ to P at the point at which the two differential cross sections (as functions of Q, Q_T and y) cross each other. In contrast to the fixed-order (dashed) curve P in Fig. 5(b), the agreement with data is improved at the lowest values of Q_T, where resummation brings the rate down, and for $Q_T = 12 - 32$ GeV, where the resummed logarithmic terms increase the rate.

The resummed predictions for the Tevatron experiments are practically insensitive to the choice of the resummation scheme and the nonperturbative model [3]. About 75% (25%) of the total rate at the Tevatron with CDF cuts imposed comes from the $q\bar{q}+qg+\bar{q}g$ ($gg+gq_S$) initial state. The fractions for the cuts used by DØ are 84% and 16%. The $gg + gq_S$ contribution falls steeply after $Q_T > 22$ GeV, because the gluon PDF decreases rapidly with parton fractional momentum x [3].

The distribution in the difference $\Delta\varphi$ of the azimuthal angles of the photons is shown in Fig. 6. As is true for the transverse momentum distribution in the limit $Q_T \to 0$, the distribution computed at fixed order is ill-defined at $\Delta\varphi = \pi$. The resummed distribution shows a larger cross section near $\Delta\varphi = 2.5$ rad, in better agreement with the data. In the region of small $\Delta\varphi \lesssim \pi/2$, the fixed-order and the resummed predictions are the same, a
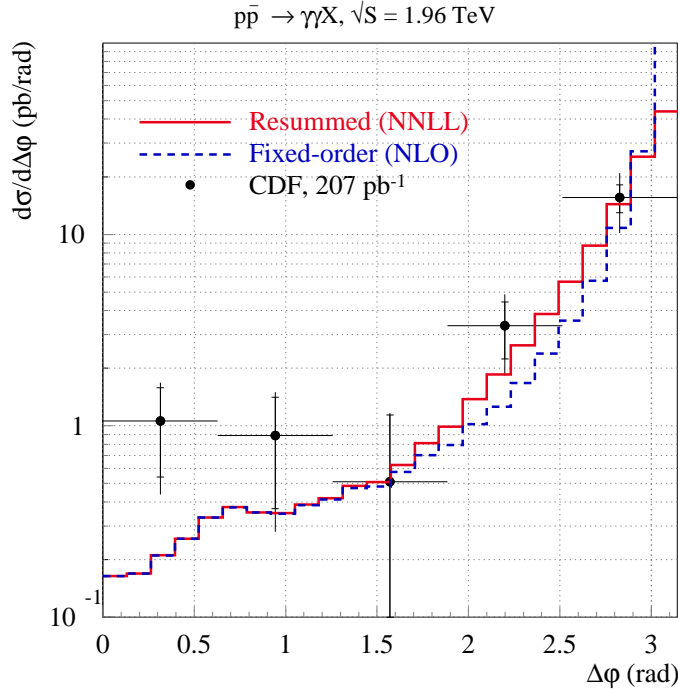
Figure 6: The difference $\Delta\varphi$ in the azimuthal angles of the two photons in the laboratory frame predicted by the resummed (solid) and fixed-order (dashed) calculations, compared to the CDF data.

result of our matching of the resummed and fixed-order distributions at mid to high values of Q_T. Although the cross section is not large in the region $\Delta\varphi < \pi/2$, there is an indication of a difference between our predictions and data in this region, a topic we address below.

3. The region $Q_T > Q$

It is evident from Fig. 3 that the $\Delta\varphi < \pi/2$ region is populated mostly by events with $Q_T > Q$. New types of radiative contributions may be present in this region, including various fragmentation contributions described in Sec. II C and enhancements at large $|\cos\theta_*|$ in the direct production rate.

While experimental isolation generally suppresses long-distance fragmentation, a greater fraction of fragmentation photons are expected to survive isolation when $\Delta\varphi < \pi/2$. Besides single-photon 'one-fragmentation' and 'two-fragmentation' contributions (with one photon per fragmenting parton), one encounters additional logarithmic singularities of the form $\log(Q/Q_T)$. We noted in Sec. II C that these logarithms are associated with the fragmentation of a parton carrying large transverse momentum Q_T into a system of small invariant mass Q [27, 28], a light $\gamma\gamma$ pair in our case. Small-Q $\gamma\gamma$ fragmentation of this kind is not implemented yet in theoretical models. Therefore, we are prepared for the possibility that both the fixed-order calculation and our resummed calculation may be deficient in the region $Q_T \gg Q$. A detailed experimental study of the region $Q_T > Q$ may offer the opportunity to measure the parton to two-photon fragmentation function $D_{\gamma\gamma}(z_1, z_2)$, provided that the

18

single-photon 'one-fragmentation' function $D_\gamma(z)$ is determined by single-photon data, and the low-Q logarithmic terms are properly resummed theoretically.

In addition to the low-Q fragmentation, the small-$\Delta\varphi$ region may be sensitive to large higher-order contributions associated with $\widehat{t}$- or $\widehat{u}$-channel exchanges in the $q\bar{q} \to \gamma\gamma$ and $gg \to \gamma\gamma$ subprocesses. In the Born processes in Figs. 1(a) and (h), the $\widehat{t}$- and $\widehat{u}$-channel singularities arise at $\cos\theta_* \approx \pm 1$ and $\Delta\varphi \approx \pi$. These singularities are excluded by the p_T^γ cuts in Eq. (23), but related residual enhancements in the NLO contributions may still persist at $|\cos\theta_*| \approx 1$ and $\Delta\varphi \to 0$, not excluded by the cuts (cf. Fig. 3). Because $|\cos\theta_*|$ is large in such events, they tend to have substantial $|\Delta y|$, so they are retained by the $\Delta R_{\gamma\gamma} > 0.3$ cut. In contrast, the low-Q fragmentation contributions tend to be abundant at small $|\Delta y|$. It may be therefore possible to distinguish between the large-$|\cos\theta_*|$ and fragmentation events at small $\Delta\varphi$ based on the distribution in $|\Delta y|$.

We expect much better agreement of our predictions with data if the selection $Q_T < Q$ is made. This selection preserves the bulk of the cross section and assures that a fair comparison is made in the region of phase space where the predictions are most valid.

4.   Fragmentation and comparison with the DIPHOX code

One way to obtain an estimate of theoretical uncertainty is to compare theoretical approaches in various parts of phase space, including small $\Delta\varphi$. We handle the collinear final-state photon singularities in the manner described in Sec. II, without including photon fragmentation functions explicitly. An alternative calculation implemented in the DIPHOX code [14] includes NLO cross sections for single-photon fragmentation processes. Neither code includes a term in which both photons are fragmentation products of the same final-state parton, i.e., the diphoton fragmentation function $D_{\gamma\gamma}(z_1, z_2)$.

In Ref. [2] we show comparisons of our predictions with those of DIPHOX along with the CDF data. Here in Fig. 7, we show analogous plots of the invariant mass and transverse momentum distributions for DØ cuts. We note that our fixed-order $q\bar{q} + qg$ contribution agrees well with the direct contribution in DIPHOX. This agreement is particularly impressive in the region of large Q_T, where both codes use the same fixed-order formalism to handle direct contributions. A contribution from the gg channel is also present in both codes, computed at LO in DIPHOX but at NLO+NNLL in our case. Since the $gg + gq_S$ contribution is not dominant (especially in the high Q_T region), this difference does not have a significant impact on the comparison.

The explicit single-photon fragmentation contributions in DIPHOX (mostly 'one-fragmentation' contribution) are quite small for the nominal hadronic energy $E_T^{iso} \sim 1$ GeV in the cone around each photon. Exceptions occur in the region $Q_T \leq E_T^{iso}$, where the fragmentation contributions to $d\sigma/dQ_T$ have logarithmic singularities, and in the $\Delta\varphi \to 0$ region, where fragmentation is comparable to the direct contributions. Our isolation prescription reproduces the integrated DIPHOX rate well for $0 \leq Q_T \leq E_T^{iso}$, leading to close agreement between the resummed and DIPHOX inclusive rates for most Q values.

Returning to the CDF measurement, we remark that the resummed and DIPHOX cross sections for the same $E_T^{iso} = 1$ GeV underestimate the data within two standard deviations for $Q \lesssim 27$ GeV, $Q_T > 25$ GeV, and $\Delta\varphi < 1$ rad (cf. the relevant figures in Ref. [2]). The DIPHOX cross section can be raised to agree with data in this "shoulder" region, if a much larger isolation energy ($E_T^{iso} = 4$ GeV) is chosen, and smaller factorization and
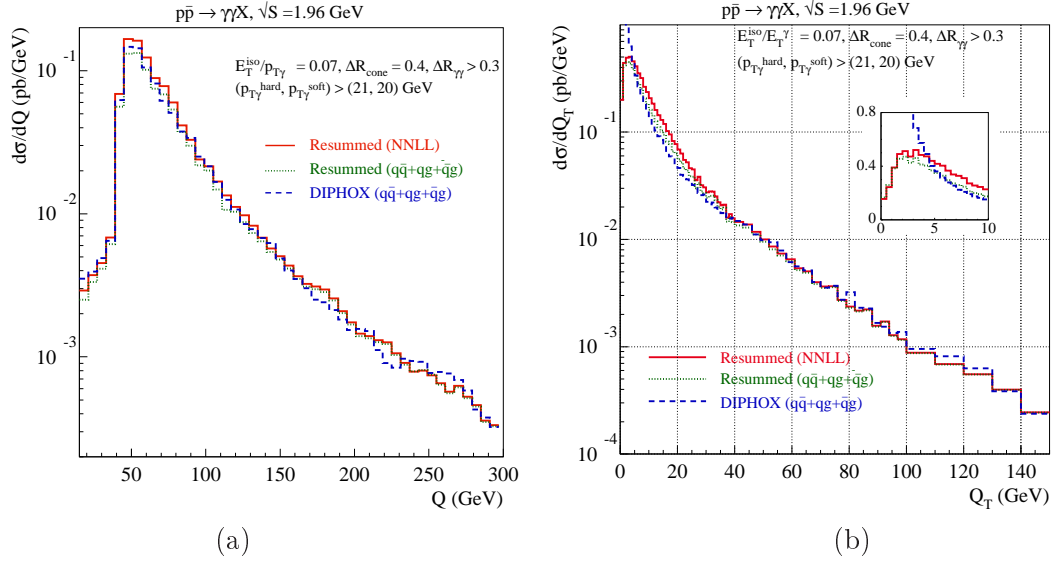
19

p̄p → γγX, √S =1.96 GeV

$E_T^{iso}/p_{T\gamma} = 0.07$, $\Delta R_{cone} = 0.4$, $\Delta R_{\gamma\gamma} > 0.3$
$(p_{T\gamma}^{hard}, p_{T\gamma}^{soft}) > (21, 20)$ GeV

Resummed (NNLL)
Resummed ($q\bar{q}+qg+\bar{q}g$)
DIPHOX ($q\bar{q}+qg+\bar{q}g$)

$d\sigma/dQ$ (pb/GeV)

Q (GeV)

(a)

p̄p → γγX, √S =1.96 GeV

$E_T^{iso}/E_T^{\gamma} = 0.07$, $\Delta R_{cone} = 0.4$, $\Delta R_{\gamma\gamma} > 0.3$
$(p_{T\gamma}^{hard}, p_{T\gamma}^{soft}) > (21, 20)$ GeV

Resummed (NNLL)
Resummed ($q\bar{q}+qg+\bar{q}g$)
DIPHOX ($q\bar{q}+qg+\bar{q}g$)

$d\sigma/dQ_T$ (pb/GeV)

Q_T (GeV)

(b)

Figure 7: Comparison of our resummed and DIPHOX predictions for (a) the invariant mass and (b) transverse momentum distributions of $\gamma\gamma$ pairs for DØ kinematic cuts. The solid curves show our resummed distributions with all channels included. The dashed and dotted curves illustrate the resummed and DIPHOX distributions in the $q\bar{q} + qg$ channel.

renormalization scales are used ($\mu_F = \mu_R = Q/2$). These are the choices made in the CDF study [1]. Since E_T^{iso} is an approximate characteristic of the experimental isolation, one might argue that both $E_T^{iso} = 1$ and 4 GeV can be appropriate in a calculation to match the conditions of the CDF measurement. The direct contribution is weakly sensitive to E_T^{iso}, while the one-fragmentation part of $d\sigma/dQ_T$ is roughly proportional to E_T^{iso} (cf. Section II C). The one-fragmentation contribution is enhanced on average by 400% if E_T^{iso} is increased in the calculation from 1 to 4 GeV. The rate in the shoulder region is enhanced further if the factorization scale μ_F is reduced.

Since the theoretical specifications for isolation and for the fragmentation contribution are admittedly approximate, we question whether great importance should be placed on the agreement of theory and experiment in the region of small $\Delta\varphi$ or in the shoulder region in the Q_T distribution. A straightforward way to reduce sensitivity to fragmentation is to require $Q > 27$ GeV or $Q_T < Q$, as discussed above. The two cuts have similar effects on the event distributions. Figure 8 shows the effects of the $Q_T < Q$ cut on the Q_T and $\Delta\varphi$ distributions. The cut $Q_T < Q$ is particularly efficient at suppressing the fragmentation Q_T shoulder (and the region of small $\Delta\varphi$ altogether), while only a small portion of the event sample is lost. This cut is especially favorable, since it constrains the comparison with data to a region where the theory is well understood and has a small uncertainty. Furthermore, with the requirement of $Q_T < Q$, the dependence of differential cross sections on the choices of isolation energy E_T^{iso} and factorization scale μ_F is greatly reduced to the typical size of higher-order corrections. We predict that if a $Q_T < Q$ cut, or a $Q > 27$ GeV cut, is applied to the Tevatron data, the enhancement at low $\Delta\varphi$ and intermediate Q_T associated with the fragmentation contribution will disappear. This is an important conclusion of our study, and we urge the CDF and DØ collaborations to apply these cuts in their future analyses of the
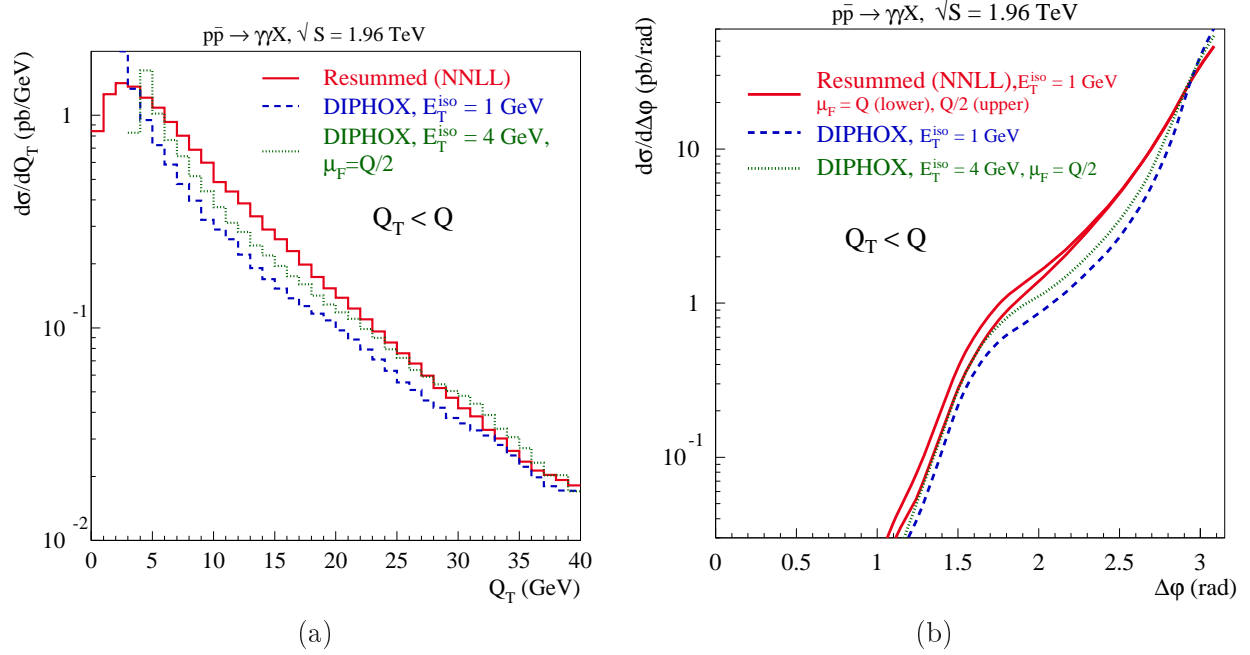
Figure 8: Predicted cross sections for diphoton production in $p\bar{p} \to \gamma\gamma X$ at $\sqrt{S} = 1.96$ TeV as a function of (a) the $\gamma\gamma$ pair transverse momentum Q_T and (b) the difference $\Delta\varphi$ in the azimuthal angles of the two photons. Our resummed predictions (solid) are shown together with DIPHOX predictions for the default isolation energy $E_T^{iso} = 1$ GeV and factorization scale $\mu_F = Q$ (dashed), and for $E_T^{iso} = 4$ GeV, $\mu_F = Q/2$ (dotted). We impose the condition $Q_T < Q$ to reduce theoretical uncertainties associated with fragmentation.

diphoton data.

5.   Average transverse momentum

An important prediction of the resummation formalism is the change of the transverse momentum distribution with the diphoton invariant mass. This dependence comes, in part, from the $\ln Q^2$ dependence in the Sudakov exponent, Eq. (17), and it is desirable to identify this feature amid other influences. In Fig. 9(a), we show normalized resummed transverse momentum distributions for various selections of the invariant mass of the photon pairs. Without kinematical constraints on the decay photons, the Q_T distribution is expected to broaden with increasing Q, and the position of the peak in $d\sigma/dQ_T$ to shift to larger Q_T values. The shift of the peak may or may not be observed in the data depending on the chosen lower cuts on p_T of the photons, which suppress the event rate at low Q and Q_T. The interplay of the Sudakov broadening of the Q_T distribution and kinematical suppression by the photon p_T cuts is reflected in the shape of $d\sigma/dQ_T$ in different Q bins.

According to dimensional analysis, the average $\langle Q_T \rangle$ in the interval $Q_T \le Q$ may be expected to behave as

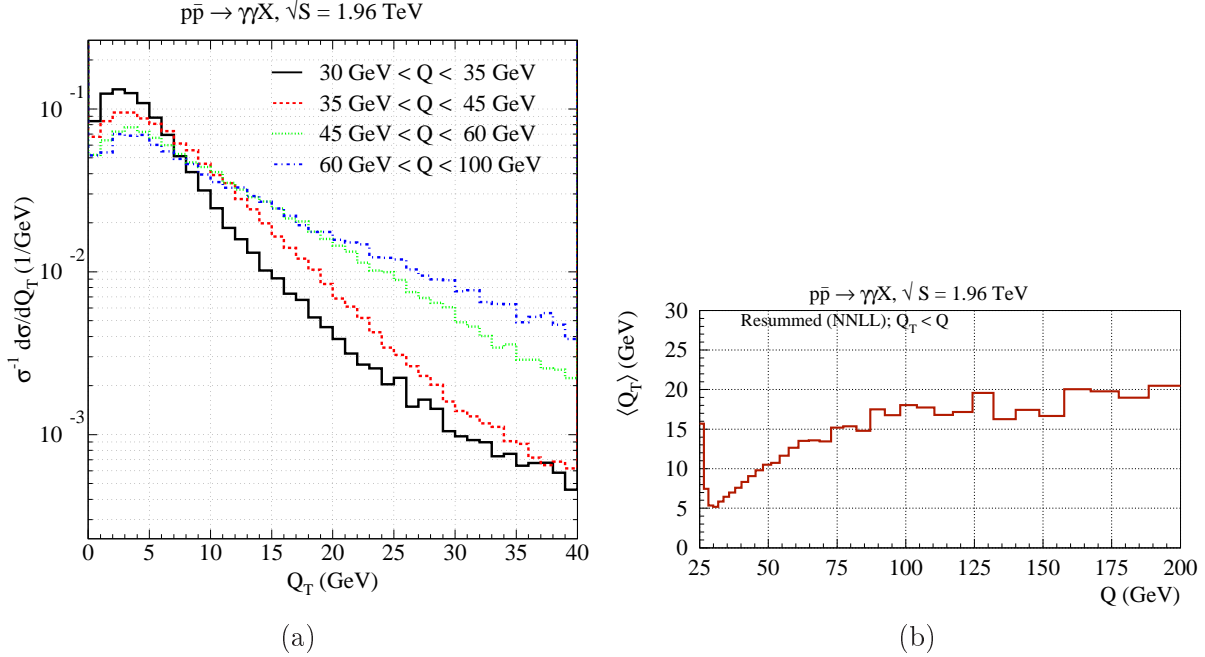$$\langle Q_T \rangle_{Q_T \le Q} = Q f(Q/\sqrt{S}), \tag{25}$$

Figure 9: (a) Resummed transverse momentum distributions of photon pairs in various invariant mass bins used in the CDF measurement, normalized to the total cross section in each Q bin. (b) The average Q_T as a function of the $\gamma\gamma$ invariant mass, computed for $Q_T < Q$.

where the scaling function $f(Q/\sqrt{S})$ reflects phase space constraints, dependence on the Sudakov logarithm, and the x dependence of the PDFs. Figure 9(b) shows our calculated diphoton mass dependence of $\langle Q_T \rangle$. The linear increase shown in Eq. (25) is observed over the range $30 < Q < 80$ GeV. For values of Q below the kinematic cutoff at about 30 GeV, the cuts shown in Fig. 3 suppress diphoton production at small Q_T, and $\langle Q_T/Q \rangle$ grows toward 1 as Q decreases (corresponding to production only at Q_T close to Q). For $Q \sim 80$ GeV and above, we see a saturation of the growth of $\langle Q_T \rangle$, a reflection of the influences of the x dependence of the PDFs and other factors. Similar saturation behavior is observed in calculations of $\langle Q_T \rangle$ in other processes [36]. It would be interesting to see a comparison of our prediction with data from the CDF and DØ collaborations.

B. Results for the LHC

1. Event selection

To obtain predictions for pp collisions at the LHC at $\sqrt{S} = 14$ TeV, we employ the cuts on the individual photons used by the ATLAS collaboration in their simulations of Higgs boson decay, $h \rightarrow \gamma\gamma$ [37]. We require

$$\text{transverse momentum } p_T^\gamma > 40 \ (25) \text{ GeV for the harder (softer) photon,} \tag{26}$$

$$\text{and rapidity } |y^\gamma| < 2.5 \text{ for each photon.} \tag{27}$$

In accord with ATLAS specifications, we impose a looser isolation restriction than for our Tevatron study, requiring less than $E_T^{iso} = 15$ GeV of hadronic and extra electromagnetic
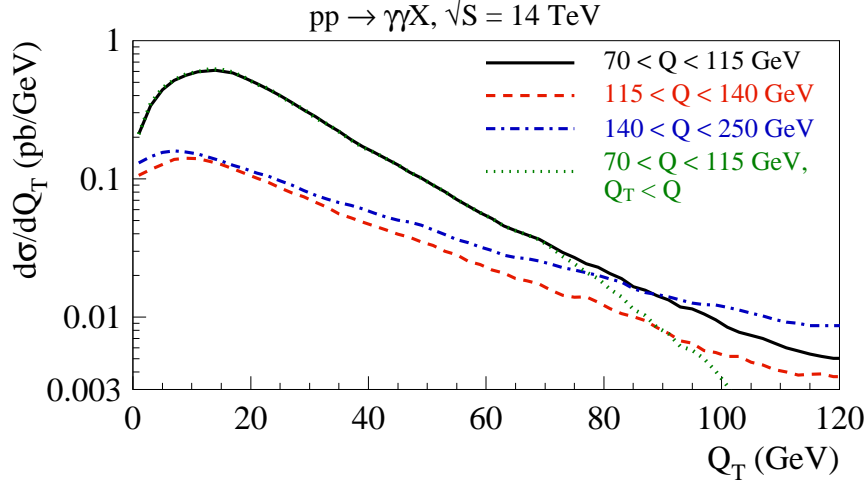
Figure 10: Resummed transverse momentum distributions of photon pairs in various invariant mass bins at the LHC. The cuts listed in Eqs. (26) and (27) are imposed.The Q_T distribution for $70 < Q < 115$ GeV with an additional constraint $Q_T < Q$ is shown as a dotted line.

transverse energy inside a $\Delta R = 0.4$ cone around each photon. We also require the separation $\Delta R_{\gamma\gamma}$ between the two isolated photons to be above 0.4.

The cuts listed above, optimized for the Higgs boson search, may require adjustments in order to test perturbative QCD predictions in the full $\gamma\gamma$ invariant mass range accessible at the LHC. The values of the p_T^γ cuts on the photons in Eq. (26) preserve a large fraction of Higgs boson events with $Q > 115$ GeV. These cuts may be too restrictive in studies of $\gamma\gamma$ production at smaller Q, considering that the two final-state photons most likely originate from a $\gamma\gamma$ pair with small Q_T and have similar values of p_T^γ of about $Q/2$. The p_T cuts interfere with the expected Sudakov broadening of Q_T distributions with increasing diphoton invariant mass, as discussed in Section III A 5. We further note that the asymmetry between the p_T^γ cuts on the harder and softer photons is necessary in a fixed-order perturbative QCD calculation, but it is not required in the resummed calculation. At a fixed order of α_s, asymmetry in the p_T^γ cuts prevents instabilities in $d\sigma/dQ$ caused by logarithmic divergences in $d\sigma/dQ_T$ at small Q_T. Such instabilities are eliminated altogether once the small-Q_T logarithmic terms are resummed to all orders of α_s. Here we do not consider alternative p_T^γ cuts, although experimental collaborations are encouraged to employ relaxed and/or symmetric cuts to increase the $\gamma\gamma$ event sample in their data analysis.

2. Resummed Q_T distributions and average transverse momentum

Figure 10 shows transverse momentum distributions of the photon pairs for various invariant masses. The average $\gamma\gamma$ transverse momentum grows with Q, as demonstrated by Fig. 11. However, the rate of the growth decreases monotonically with Q, for similar reasons as at the Tevatron.

The $\gamma\gamma$ distributions in Q and $\Delta\varphi$ for different combinations of scattering subchannels and choices of theoretical parameters are discussed in Refs. [2, 3]. In all ranges of Q, the $\gamma\gamma$ production rate is dominated by a large qg contribution, accounting for about 50% of the
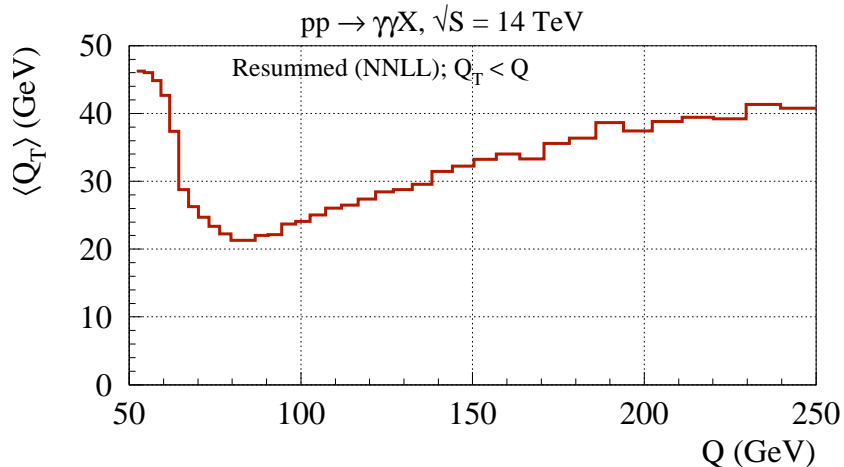
Figure 11: The average Q_T at the LHC as a function of the $\gamma\gamma$ invariant mass Q.

fixed-order (NLO) rate. Although this number depends on the choice of the factorization scheme and scale, and, on the other hand, separate treatment of the $q\bar{q}$ and qg cross sections is not meaningful in the resummation calculation [3], it nonetheless reflects, in a crude way, the increased relative importance of the qg cross section. The $gg + gq_S$ channel contributes about 25% at $Q \sim 80$ GeV (the location of the cutoff in $d\sigma/dQ$ due to the cuts on p_T^γ) and less at larger Q. As at the Tevatron, the dependence of the cross sections on the resummation scheme is small [3]. The dependence on the nonperturbative model can also be neglected, as long as the nonperturbative function does not vary strongly with x [3].

3. Final-state fragmentation and comparison with DIPHOX

The impact of the final-state fragmentation at the LHC can be evaluated if we compare our results with DIPHOX predictions. The transverse momentum and invariant mass distributions in the $q\bar{q} + qg$ channel from the two approaches are shown in Fig. 12. In both calculations, quasi-experimental isolation removes direct NLO events with collinear final-state photons and partons when $Q_T > E_T^{iso} = 15$ GeV, but not when Q_T is below E_T^{iso}.

Concentrating first on $\gamma\gamma$ events with $Q_T > E_T^{iso}$, we observe that, at $Q_T > 80$ GeV, the resummed $q\bar{q}+qg$ cross section reduces to the direct fixed-order cross section, evaluated in the same way as in the DIPHOX code. Our resummed and the direct DIPHOX cross sections, shown as solid and dashed curves, respectively, in Fig. 12(a) consequently agree well at large Q_T. At smaller Q_T, the resummed cross section is enhanced by towers of higher-order logarithmic contributions. On the other hand, the full $q\bar{q} + qg$ DIPHOX rate (shown as a dotted line) also includes single-photon fragmentation contributions, which add to the direct production cross section. For the nominal isolation parameters, the explicit fragmentation contribution constitutes about 25% of the full DIPHOX rate for $60 < Q_T < 120$ GeV. Its magnitude increases approximately linearly with the assumed E_T^{iso} value.

For $Q_T < E_T^{iso}$, the final-state collinear region of the direct contribution is regulated by the collinear subtraction prescription adopted in the resummation calculation, whereas
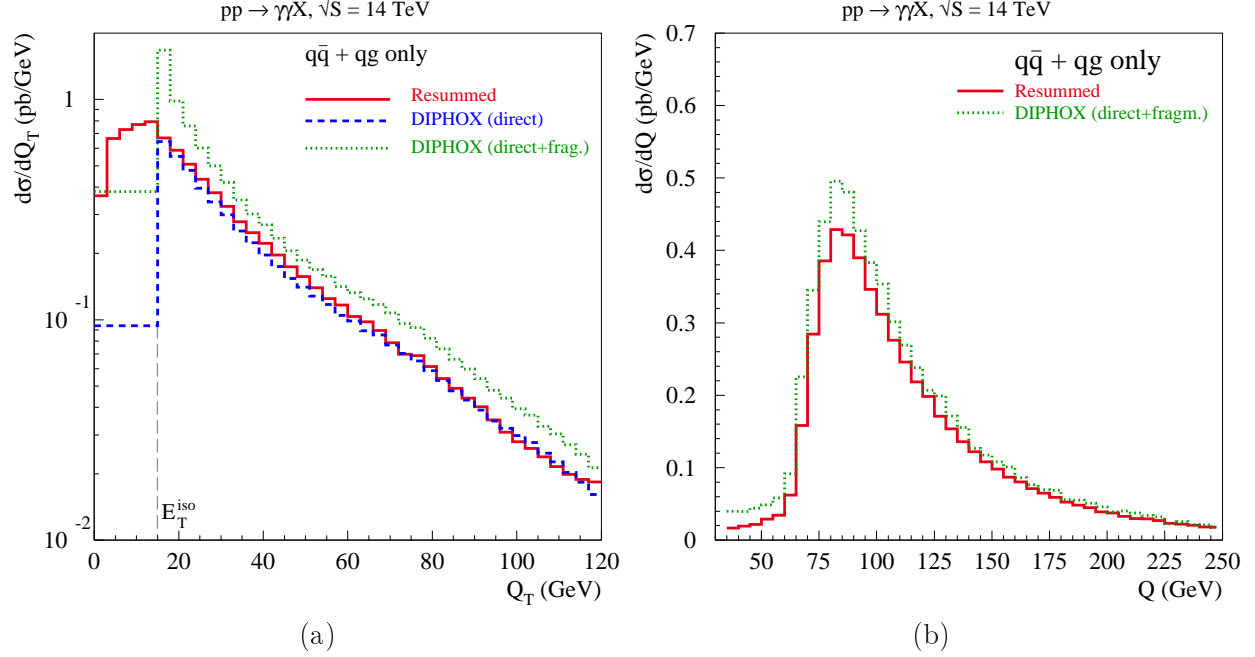
24

Figure 12: Transverse momentum and invariant mass distributions $d\sigma/dQ$ in the $q\bar{q} + qg$ channel obtained in the resummation (solid) and DIPHOX (dotted) calculations.

the fragmentation singularity is subtracted from the direct contribution and replaced by photon fragmentation functions in the DIPHOX calculation. Subtraction of singularities in DIPHOX introduces integrable singularities in $d\sigma/dQ_T$ at different values of Q_T below E_T^{iso}. The origin of the final-state logarithmic singularities at values of Q_T below E_T^{iso} is discussed in Refs. [22, 23, 24]. For $Q_T < E_T^{iso}$, the DIPHOX curves represent the average over singular contributions in this Q_T interval.

After the fragmentation singularity is subtracted, the DIPHOX direct contribution (dashed line) is on average below our resummed $q\bar{q} + qg$ rate (solid line) over most of the range of Q_T shown in Fig. 12(a). After integration over all Q_T, our resummed and DIPHOX $q\bar{q} + qg$ cross sections agree within 10-20% at most values of Q (cf. Fig. 12(b)), with our resummed rate being below the DIPHOX rate at all Q. The largest difference occurs at the lowest values of Q (below the cutoff), where the rates can differ by a factor of 2. In this region, corresponding to diphoton events with small $\Delta\varphi$ and Q_T larger than Q, the photon fragmentation contributions included in the DIPHOX calculation are large in comparison to the direct rate. Finally, we note that the integrated rate in DIPHOX is more stable with respect to variations in E_T^{iso} than the differential distributions in DIPHOX, because E_T^{iso} dependence for $Q_T > E_T^{iso}$ is canceled to a good degree by E_T^{iso} dependence for $Q_T < E_T^{iso}$.

To obtain the final $\gamma\gamma$ production cross sections, after inclusion of all channels, we combine the respective $q\bar{q} + qg$ results with the resummed NLO $gg + gq_S$ cross section in our case and with the LO gg cross section in the DIPHOX case. The distributions in the $\gamma\gamma$ invariant mass Q, the transverse momentum Q_T, and the azimuthal angle separation $\Delta\varphi$ in the lab frame are shown in Fig. 13. For the cuts chosen, the LO gg and the resummed $gg + gq_S$ total rates constitute about 9% and 20% of the total rate. The resummed and DIPHOX invariant mass distributions (Fig. 13(a)) are brought closer to one another as a result of the inclusion
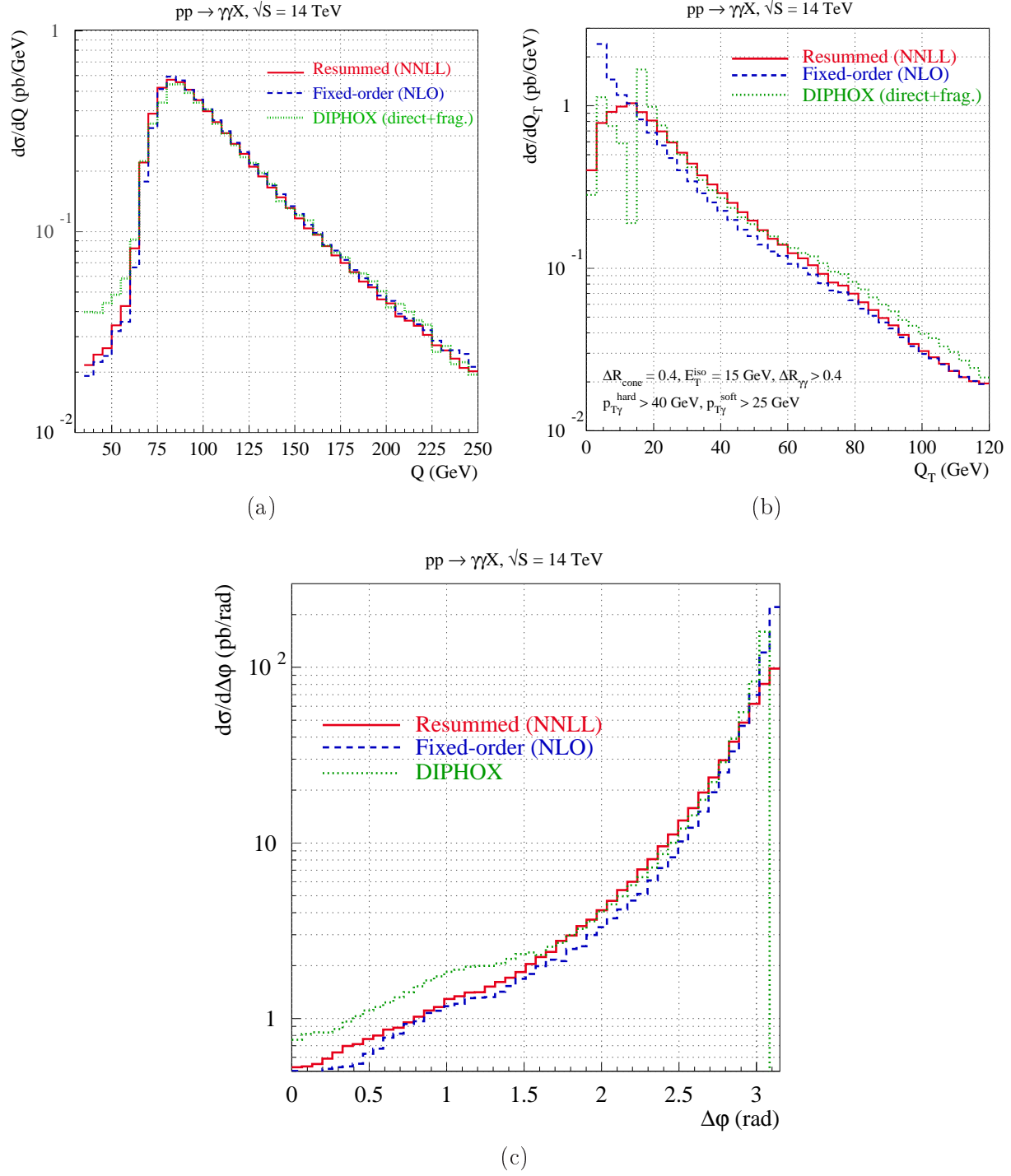
Figure 13: Invariant mass, transverse momentum, and $\Delta\varphi$ distributions from our resummed calculation and from DIPHOX at the LHC. We show our fixed-order (dashed) and resummed (solid) distributions. All initial states are included in both calculations, and the single-γ fragmentation contributions are included in DIPHOX.
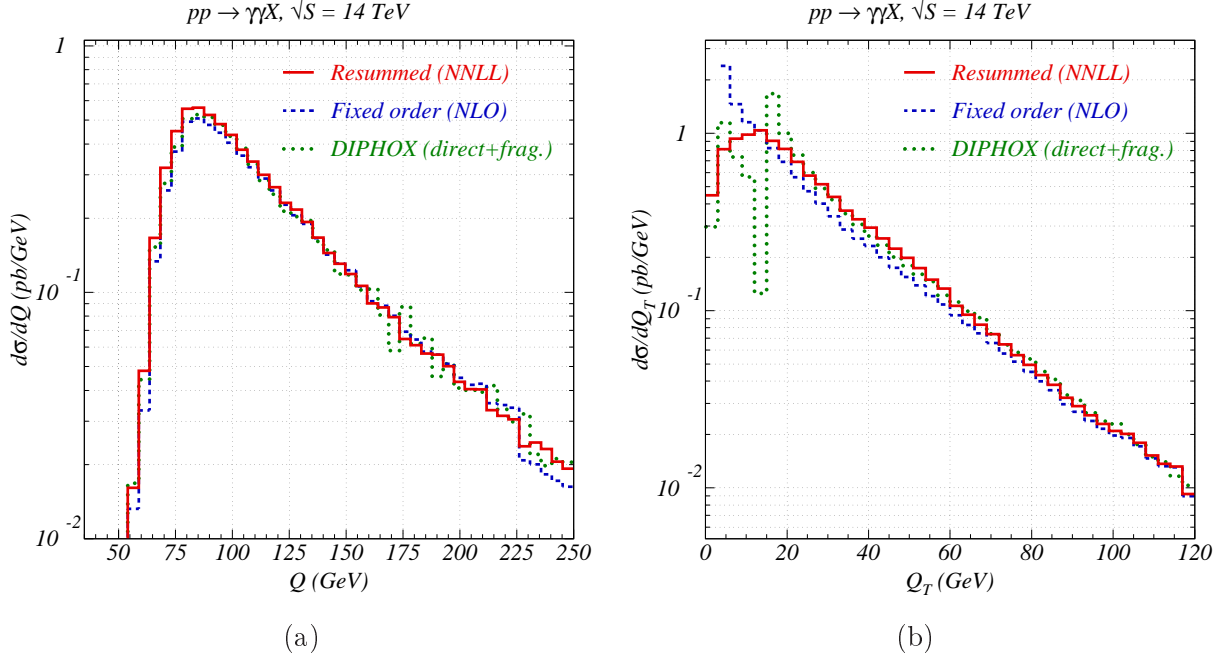
Figure 14: Invariant mass and transverse momentum distributions from our resummed, NLO, and DIPHOX calculations at the LHC, with the $Q_T < Q$ constraint imposed.

of the $gg + gq_S$ contribution in the resummed calculation. For $Q_T \neq 0$, the full DIPHOX Q_T distribution in Fig. 13(b) is determined entirely by direct plus fragmentation contributions (the same as in Fig. 12(a)), because the LO gg cross section contributes at $Q_T = 0$ only. In contrast, our resummed $gg + gq_S$ contribution modifies the event rate at all Q_T.

The resummed and DIPHOX rates are in a reasonable agreement for $1.5 \lesssim \Delta\varphi \lesssim 2.5$, as shown in Fig. 13(c). In the $\Delta\varphi \to \pi$ limit, the fixed-order rates in DIPHOX diverge because of the singularities at small Q_T, while our resummed rate yields a finite value. For $\Delta\varphi < 1.5$, the DIPHOX cross section is enhanced by photon fragmentation contributions. As at the energy of the Tevatron, theoretical uncertainties are greater at small $\Delta\varphi$.

Predictions are most reliable when $Q_T < Q$ (and the angles θ_* and φ_* are away from 0 or π). With the $Q_T < Q$ cut imposed, the uncertain large-Q_T photon fragmentation contributions are suppressed, and the resummed and DIPHOX cross sections agree well at large Q_T (cf. Fig. 14(b)). The Q_T distribution in the interval $70 < Q < 115$ GeV with the $Q_T < Q$ constraint is shown in Fig. 10 by a dotted curve. Distributions in the other two mass bins in Fig. 10 are essentially not affected by this cut in the Q_T range presented.

Our calculation captures the dominant contributions to $\gamma\gamma$ production at the LHC. However, as we noted, direct qg scattering, evaluated at order $\mathcal{O}(\alpha_s)$ in our calculation, is the leading scattering channel in the region relevant for the Higgs boson search at the LHC. It is important to emphasize that the final-state collinear radiation is not the main reason behind the enhancement of the qg rate, which is increased predominantly by contributions from non-singular phase space regions. Consequently, the $q\bar{q} + qg$ direct rate is only weakly sensitive to adjustments in the isolation parameters E_T^{iso} and ΔR [10]. The unknown $\mathcal{O}(\alpha_s^2)$ contributions to qg scattering may be non-negligible, and it would be valuable to compute them in the future when LHC data are available.
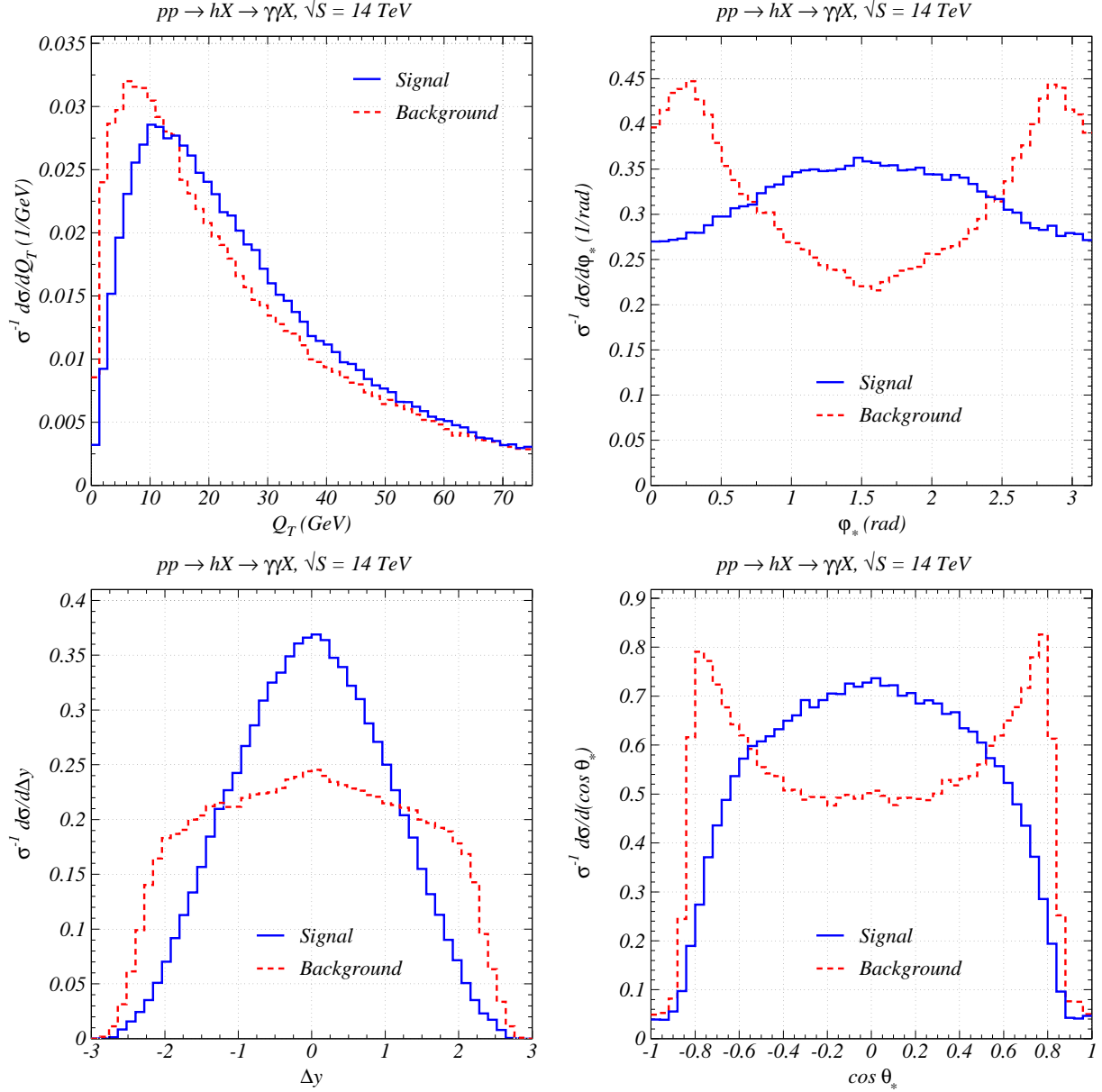
27

Figure 15: Comparison of the normalized Higgs boson signal and diphoton background distributions at the LHC, both computed at NNLL accuracy. The Higgs boson mass is taken to be $m_H = 130$ GeV, and the background is calculated for $128 < Q < 132$ GeV.

C. Comparison with Higgs boson signal distributions

We highlight some similarities and differences between the production spectra for the Higgs boson signal and the QCD background discussed in this paper. We focus on the diphoton decay mode of a SM Higgs boson produced from the dominant gluon-fusion mechanism, $gg \rightarrow h^0 \rightarrow \gamma\gamma$, where the Higgs boson production cross section is calculated at the same order of precision as the QCD continuum background. We include initial-state QCD contributions at $O(\alpha_s^3)$ (NLO) and resummed contributions at NNLL accuracy. These con-

tributions are also coded in RESBOS [38], and we can apply the same cuts on the momenta of the photons to the signal and background. Our findings should remain broadly applicable after the NNLO corrections to Higgs boson production [39, 40] are included. We compute the background in the range $128 < Q < 132$ GeV, and the signal at a fixed Higgs boson mass $m_H = 130$ GeV. We impose the kinematic selection $Q_T < Q$, but its influence is not important at the large values of diphoton mass of interest here.

The cross section times branching ratio for the Higgs boson signal is substantially smaller than the QCD continuum. To better illustrate their differences, Fig. 15 presents distributions normalized to the respective total rates. The top-left panel shows normalized transverse momentum distributions of photon pairs. The signal and background peak at about 12 and 5 GeV, respectively. The average values of Q_T are 26 and 23 GeV, computed over the range 0 to 75 GeV.

Differences in the shapes of these Q_T spectra can be attributed to the different structure of the leading terms in the initial-state Sudakov exponents and to the effects of final-state photon fragmentation. The Higgs boson signal is controlled by the characteristics of the $gg+gq_S$ initial state, whereas the continuum is controlled primarily by the $q\bar{q}+qg$ initial state. Because the dominant Sudakov coefficient $\mathcal{A}_q^{(k)} \propto C_F$ in the $q\bar{q}$ case is smaller than $\mathcal{A}_g^{(k)} = (C_A/C_F)\mathcal{A}_q^{(k)}$ in the gg case, the resummed $q\bar{q} + qg$ initial-state radiation produces narrower Q_T distributions than $gg + gq_S$ initial-state radiation. About 80% of the diphoton rate is provided by the $q\bar{q} + qg$ channel, implying a narrower Q_T distribution of the background, if based on the value of $\mathcal{A}^{(k)}$ alone.

The continuum background contribution is also enhanced by final-state radiation in qg scattering. The Q_T profile of the final-state collinear terms depends more on the isolation model (including E_T^{iso} and ΔR) than on the initial-state Sudakov exponent. For the nominal ATLAS cuts, the final-state collinear contribution in our calculation hardens the background Q_T distribution, diminishing its difference from the Higgs boson signal distribution. More effective isolation may reduce the impact of the final-state radiation on Q_T distributions.

Another difference between the signal and continuum is observed in the distribution in the azimuthal angle of the photons, such as the angle φ_* in the Collins-Soper frame shown in the top-right panel of Fig. 15. This distribution is qualitatively the same if integrated over all Q_T, as in Fig. 15, or integrated above some minimal Q_T value, as in an experimental measurement. Without isolation imposed, the spin-0 Higgs boson signal must be flat in φ_*, but the QCD background peaks toward $\varphi_* = 0$ and π (i.e., $\sin\varphi_* = 0$) as a result of the final-state qg singularity.[2, 3] Isolation cuts suppress both the signal and the background for $\sin\varphi_* < \sin\Delta R$. The result is a signal distribution with a broad peak near $\varphi_* = \pi/2$, while the background favors values of φ_* near 0 and π. A selection of events with φ_* in the vicinity of $\pi/2$, and Q_T large enough, helps to reduce the impact of the qg background. In the lab frame, a related distribution is in the variable $|\varphi_{3T} - \varphi_{4T}|$, where φ_{iT} is the azimuthal angle between $\vec{p}_T^{\gamma_i}$ and $\vec{Q}_T$. The signal (background) processes tend to have more events with large

---

[2] By definition, the recoil parton 5 always lies in the Oxz plane (has zero azimuthal angle) in the Collins-Soper frame. For the final-state singularity to occur at NLO, the photons should be in the same plane with 5, i.e., have $\sin\varphi_* = 0$.

[3] One of the resummed structure functions for the gg background is modulated by $\cos 2\varphi_*$ (see Sec. II B), but we neglect this modulation in our present calculation.

(small) magnitude of $|\varphi_{3T} - \varphi_{4T}|$.

A third potential discriminator between the signal and background is the difference in the rapidities $\Delta y = y_{hard} - y_{soft}$ of the photons with harder and softer values of p_T^γ in the lab frame, calculated on an event by event basis. This distribution is displayed in the lower-left frame of Fig. 15. The background distribution peaks at the origin, while the signal is almost flat over a wide range of Δy. Different spin correlations in the decay of a spin-0 Higgs boson from those characteristic of QCD background processes are the source of this distinction. Discrimination based on this difference can improve the statistical significance of the signal [10]. We note that our resummed calculation does not exhibit the kinematic singularity at $\Delta y \approx 2$ present in the finite-order cross section and obvious in Fig. 10 of Ref. [10], where the distribution with respect to $y^* \equiv \Delta y/2$ is shown. The discontinuity in $d\sigma/dQ_T$ caused by the finite-order approximation is resummed in our calculation, yielding a smooth result.

The rapidity difference is related to the scattering angle in the Collins-Soper frame: $\tanh(\Delta y/2) = \cos\theta_*$ when Q_T is zero. The $\cos\theta_*$ distribution is shown in the lower-right frame of Fig. 15. The difference between the signal and background rates is even more pronounced in this variable, clearly expressing the difference in the spin correlations of the systems producing the photons.

A comparison of Q_T distributions in the top-left panel of Fig. 15 suggests that the signal versus background ratio would be enhanced if a cut is made to restrict $Q_T > 10$ GeV. After applying this cut, we may again examine the distributions in the rapidity difference of the two photons, the scattering angle in the Collins-Soper frame, and the azimuthal angle distribution of the photons in the Collins-Soper frame. The results are qualitatively similar to those in Fig. 15 and are not shown here. A more efficient procedure to increase the Higgs boson discovery significance is to apply a simultaneous likelihood analysis to several kinematic distributions. Based on the present discussion, we would argue that the resummed Q_T, φ_*, and $\cos\theta_*$ distributions are good discriminators between the Higgs boson signal and background in such an analysis.

IV. CONCLUSIONS

The theoretical study of continuum diphoton production in hadron collisions is interesting and valuable for several reasons: there are data from the CDF and DØ collaborations at Fermilab with the promise of larger event samples; there are new theoretical challenges associated with all-orders soft-gluon resummation of two-loop amplitudes; and continuum diphotons are a large standard-model background above which one may observe the products of Higgs boson decay into a pair of photons at the LHC.

In this paper and Refs. [2, 3], we present our calculation of the fully differential cross section $d\sigma/(dQdQ_T dy d\Omega_*)$ as a function of the mass Q, transverse momentum Q_T, and rapidity y of the diphoton system, and of the polar and azimuthal angles of the individual photons in the diphoton rest frame. Our basic QCD hard-scattering subprocesses are all computed at next-to-leading order (NLO) in the strong coupling strength α_s, and we include the state-of-art resummation of initial-state gluon radiation to all orders in α_s, valid to next-to-next-to-leading logarithmic accuracy (NNLL). Resummation is essential for a realistic and reliable calculation of the Q_T dependence in the region of small and intermediate values of Q_T, where the cross section is greatest. It is also needed for stable estimates of the effects of

experimental acceptance on distributions in the diphoton invariant mass and other variables.

Our analytical results are included in a fully updated RESBOS code [31, 32]. This numerical program allows us to impose selections on the transverse momenta and angles of the final photons, in order to match those employed by the CDF and DØ collaborations, as well as those anticipated in experiments at the LHC. Our predictions are especially pertinent in the region $Q_T \lesssim Q$. We show that our results at the Tevatron and at the LHC are insensitive to the choice of the resummation scheme and of the nonperturbative functions required by the integration into the region of large impact parameter.

The published collider data are presented in the form of singly differential distributions. We follow suit in order to make comparisons, and we find excellent agreement with data, as shown in Sec. III. We recommend that more differential studies be made, and, to motivate these, we present predictions for the changes expected in the Q_T distribution as a function of mass Q, and for the dependence of the mean transverse momentum on Q.

We make predictions for continuum diphoton mass, transverse momentum, and angular distributions at the energy of the LHC. Moreover, we contrast in Fig. 15 the shapes of some of these distributions with those expected from the decay of a Higgs boson. The distinct features of the signal and background suggest that that the Higgs boson discovery significance can be increased via a simultaneous likelihood analysis of several kinematic distributions, particularly the resummed Q_T, φ_*, and $\cos\theta_*$ distributions.

Another approach to the computation of continuum diphoton production is presented by the DIPHOX collaboration [14]. This calculation includes both the direct production of photons from hard-scattering processes and the photons produced from fragmentation of (anti-)quarks or gluons. It is valid at NLO, except for the gg subprocess, which is included at leading order only. The DIPHOX code is useful for rates integrated over transverse momentum, but it is not designed to predict the transverse momentum distribution or other distributions sensitive to the region in which the transverse momentum of the diphoton pair is small. Compared to a fixed-order calculation, such as direct photon pair calculation in DIPHOX, our calculation improves the theoretical prediction for event distributions which are sensitive to the region of low Q_T. Furthermore, our calculation includes the NLO contribution from the combined $gg + gq_S$ channel, leading to more accurate predictions at the LHC, where the $gg + gq_S$ contribution is generally not small.

Only *isolated*, not inclusive, photons are identified experimentally. While it is straightforward to define an isolated photon in a given experiment, it is challenging to devise a theoretical prescription that can match the experimental definition, short of first understanding the long-distance dynamics of QCD. The isolated diphoton production rate is modeled in the DIPHOX code by including explicit photon fragmentation function contributions at NLO accuracy. A shortcoming of this approach (as well as of our method for treating isolation) is that one cannot accurately represent photon fragmentation without including final-state parton showering in the presence of isolation constraints. There is inevitable ambiguity and uncertainty in the choice of the "isolation energy" used to define an isolated photon theoretically for comparison with the isolated photon measured experimentally. As shown in Sec. III, the DIPHOX cross section can vary by a large factor in some regions of phase space at the Tevatron when E_T^{iso} is changed from $1\,\mathrm{GeV}$ to $4\,\mathrm{GeV}$.

Our approach is to concentrate on physical observables which are less sensitive to the fragmentation contributions. We apply the "collinear subtraction" prescription or the "smooth-cone isolation" prescription to define an isolated photon in our calculation. We find good

agreement with the data, except in the region with small Q and $\Delta\varphi < \pi/2$, consistent with our theoretical expectation that higher-order direct photon production and photon fragmentation contributions can strongly modify the rate of diphoton pairs in this region. We suggest that much better agreement with current and future data will be obtained if an addition requirement of $Q_T < Q$ is applied. With this cut, the fragmentation contributions are largely suppressed. With the cut $Q_T < Q$ cut applied to the Tevatron data, the enhancement at low $\Delta\varphi$ and intermediate Q_T (the shoulder region) should disappear. We urge the CDF and DØ collaborations to apply these cuts in future analyses of the diphoton data.

In our calculation, we identify an interesting spin-flip contribution (with $\cos 2\varphi_*$ dependence) in the gg channel, cf. Ref. [3], and we suggest that measurements be made of the distribution of φ_* as a function of Q_T. All-orders resummation of the gluon spin-flip contribution may be needed when a larger statistical sample of diphoton data is available.

The contributions from $qg + \bar{q}g$ processes become more important at the LHC than at the Tevatron, and calculations at a higher order of precision may be warranted eventually. To improve the theoretical prediction in the region of phase space with $Q_T < E_T^{iso}$ and $\varphi_* \sim 0$ or π, a joint resummation calculation is needed in which the effects of both the initial- and final-state multiple parton emissions are treated simultaneously.

Although we emphasize that better agreement of our predictions with data should be apparent if the selection $Q_T < Q$ is made, we also point out that the region $Q_T > Q$ should manifest very interesting physics of a different sort. Additional logarithmic singularities of the form $\log(Q/Q_T)$ are encountered in the region $Q_T \gg Q$. These logarithms are associated with the fragmentation of a parton carrying large transverse momentum Q_T into a system of small invariant mass Q [27, 28], a light $\gamma\gamma$ pair in our case. Small-Q $\gamma\gamma$ fragmentation of this kind is not implemented yet in theoretical models. Experimental study of the region $Q_T \gg Q$ may offer the opportunity to measure the parton to two-photon fragmentation function $D_{\gamma\gamma}(z_1, z_2)$.

Acknowledgments

Appendix A: SUMMARY OF PERTURBATIVE COEFFICIENTS

In this appendix we present an overview of the perturbative QCD expressions for the resummed and asymptotic cross sections used in our computation.

The functions $\mathcal{A}_a(C_1, \bar{\mu})$, $\mathcal{B}_a(C_1, C_2, \bar{\mu})$, $\mathcal{C}_{a/a_1}(x, b; C_1/C_2, \mu)$, and $h_a(Q, \theta_*)$ are introduced in Sec. II. These functions are derived as perturbative expansions in the small parameter

α_s/π:

$$\mathcal{A}_a(C_1, \bar{\mu}) = \sum_{n=1}^{\infty} \mathcal{A}_a^{(n)}(C_1) \left(\frac{\alpha_s(\bar{\mu})}{\pi} \right)^n ; \quad \mathcal{B}_a(C_1, C_2, \bar{\mu}) = \sum_{n=1}^{\infty} \mathcal{B}_a^{(n)}(C_1, C_2) \left(\frac{\alpha_s(\bar{\mu})}{\pi} \right)^n ;$$

$$\mathcal{C}_{a/a_1}\left(x, b; \frac{C_1}{C_2}, \mu \right) = \sum_{n=0}^{\infty} \mathcal{C}_{a/a_1}^{(n)}(x, b\mu, \frac{C_1}{C_2}) \left(\frac{\alpha_s(\mu)}{\pi} \right)^n ; \quad h_a(Q, \theta_*) = \sum_{n=0}^{\infty} h_a^{(n)}(\theta_*) \left(\frac{\alpha_s(Q)}{\pi} \right)^n .$$

The value of a perturbative coefficient $F^{(n)}$ for a set of scales C_1/b and $C_2 Q$ can be expressed in terms of its value $F^{(n,c)}$ obtained for the "canonical" combination $C_1 = c_0$ and $C_2 = 1$. Here $c_0 \equiv 2e^{-\gamma_E} \approx 1.123$, where $\gamma_E = 0.5772\ldots$ is the Euler constant. The relationships between $F^{(n)}$ and $F^{(n,c)}$ take the form

$$\mathcal{A}_a^{(1)}(C_1) = \mathcal{A}_a^{(1,c)}; \tag{A1}$$

$$\mathcal{A}_a^{(2)}(C_1) = \mathcal{A}_a^{(2,c)} - \mathcal{A}_a^{(1,c)} \beta_0 \ln \frac{c_0}{C_1}; \tag{A2}$$

$$\mathcal{A}_a^{(3)}(C_1) = \mathcal{A}_a^{(3,c)} - 2\mathcal{A}_a^{(2,c)} \beta_0 \ln \frac{c_0}{C_1} - \frac{\mathcal{A}_a^{(1,c)}}{2} \beta_1 \ln \frac{c_0}{C_1} + \mathcal{A}_a^{(1,c)} \beta_0^2 \left(\ln \frac{c_0}{C_1} \right)^2 ; \tag{A3}$$

$$\mathcal{B}_a^{(1)}(C_1, C_2) = \mathcal{B}_a^{(1,c)} - \mathcal{A}_a^{(1,c)} \ln \frac{c_0^2 C_2^2}{C_1^2}; \tag{A4}$$

$$\mathcal{B}_a^{(2)}(C_1, C_2) = \mathcal{B}_a^{(2,c)} - \mathcal{A}_a^{(2,c)} \ln \frac{c_0^2 C_2^2}{C_1^2}$$

$$+ \beta_0 \left[\mathcal{A}_a^{(1,c)} \ln^2 \frac{c_0}{C_1} + \mathcal{B}_a^{(1,c)} \ln C_2 - \mathcal{A}_a^{(1,c)} \ln^2 C_2 \right]; \tag{A5}$$

$$\mathcal{C}_{a/a_1}^{(1)}(x, b\mu, \frac{C_1}{C_2}) = \mathcal{C}_{a/a_1}^{(1,c)}(x) + \delta_{aa_1} \delta(1-x) \left(\frac{\mathcal{B}_a^{(1,c)}}{2} \ln \frac{c_0^2 C_2^2}{C_1^2} - \frac{\mathcal{A}_a^{(1,c)}}{4} \left(\ln \frac{c_0^2 C_2^2}{C_1^2} \right)^2 \right)$$

$$- P_{a/a_1}(x) \ln \frac{\mu b}{c_0}. \tag{A6}$$

They depend on the QCD beta-function coefficients $\beta_0 = (11N_c - 2N_f)/6$, $\beta_1 = (17N_c^2 - 5N_c N_f - 3C_F N_f)/6$ for N_c colors and N_f active quark flavors, with $C_F = (N_c^2 - 1)/(2N_c) = 4/3$ for $N_c = 3$. The relevant $\mathcal{O}(\alpha_s)$ splitting functions $P_{a/a_1}(x)$ are

$$P_{q/q} = C_F \left(\frac{1 + z^2}{1 - x} \right)_+ ; \quad P_{q/g} = \frac{1}{2}(1 + 2x + 2x^2); \quad P_{g/qs} = C_F \frac{(1-x)^2 + 1}{x}; \tag{A7}$$

$$P_{g/g} = 2C_A \left[\frac{x}{(1-x)_+} + \frac{1-x}{x} + x(1-x) \right] + \beta_0 \delta(1-x). \tag{A8}$$

The coefficients $h^{(1)}(\theta_*)$, $\mathcal{B}^{(2)}$, and $\mathcal{C}^{(1)}$ depend on the resummation scheme. The hard-scattering function is

$$h_a(Q, \theta_*) = 1 + \delta_s \frac{\alpha_s(Q)}{\pi} \frac{\mathcal{V}_a(\theta_*)}{4} + ..., \tag{A9}$$

where $\delta_s = 0$ in the CSS scheme and $\delta_s = 1$ in the CFG scheme. The functions $\mathcal{V}_q(\theta_*)$ for $q\bar{q} \to \gamma\gamma$ scattering and $\mathcal{V}_g(\theta_*)$ for $gg \to \gamma\gamma$ scattering are derived in Refs. [12] and [13], respectively.

For the $q\bar{q} + qg$ initial state, we obtain the following expressions for the coefficients $\mathcal{A}$, $\mathcal{B}$, and $\mathcal{C}$:

$$\mathcal{A}_q^{(1,c)} = C_F;$$

$$\mathcal{A}_q^{(2,c)} = C_F \left[\left(\frac{67}{36} - \frac{\pi^2}{12} \right) C_A - \frac{5}{9} T_R N_f \right]; \tag{A10}$$

$$\mathcal{A}_q^{(3,c)} = \frac{C_F^2 N_f}{2} \left(\zeta(3) - \frac{55}{48} \right) - \frac{C_F N_f^2}{108} + C_A^2 C_F \left(\frac{11\zeta(3)}{24} + \frac{11\pi^4}{720} - \frac{67\pi^2}{216} + \frac{245}{96} \right)$$
$$+ C_A C_F N_f \left(-\frac{7\zeta(3)}{12} + \frac{5\pi^2}{108} - \frac{209}{432} \right);$$

$$\mathcal{B}_q^{(1,c)} = -\frac{3}{2} C_F;$$

$$\mathcal{B}_q^{(2,c)} = -\frac{1}{2} \left[C_F^2 \left(\frac{3}{8} - \frac{\pi^2}{2} + 6\zeta(3) \right) + C_F C_A \left(\frac{17}{24} + \frac{11\pi^2}{18} - 3\zeta(3) \right) \right.$$
$$\left. - C_F N_f T_R \left(\frac{1}{6} + \frac{2\pi^2}{9} \right) \right] + \beta_0 \left[\frac{C_F \pi^2}{12} + (1 - \delta_s) \frac{\mathcal{V}_q(\theta_*)}{4} \right];$$

$$\mathcal{C}_{j/k}^{(0)}(x) = \delta_{jk}\delta(1-x); \ \mathcal{C}_{j/g}^{(0)}(x) = 0;$$

$$\mathcal{C}_{j/k}^{(1,c)}(x) = \delta_{jk} \left\{ \frac{C_F}{2}(1-x) + \delta(1-x)(1-\delta_s)\frac{\mathcal{V}_q(\theta_*)}{4} \right\};$$

$$\mathcal{C}_{j/g}^{(1,c)}(x) = \frac{1}{2} x(1-x). \tag{A11}$$

Here $C_A = N_c$, $T_R = 1/2$, and the Riemann constant $\zeta(3) = 1.202\dots$. The $\mathcal{C}$ functions are given for $j, k = u, \bar{u}, d, \bar{d}, \dots$. These coefficients are taken from [12, 42, 43].

Similarly, the $\mathcal{A}$, $\mathcal{B}$, and $\mathcal{C}$ coefficients in the $gg + gq_S$ channel are

$$\mathcal{A}_g^{(k,c)} = (C_A/C_F)\mathcal{A}_q^{(k,c)}, \ \text{for } k = 1, 2, 3;$$

$$\mathcal{B}_g^{(1,c)} = -\beta_0;$$

$$\mathcal{B}_g^{(2,c)} = -\frac{1}{2} \left[C_A^2 \left(\frac{8}{3} + 3\zeta(3) \right) - C_F T_R N_f - \frac{4}{3} C_A T_R N_f \right] + \beta_0 \left[\frac{C_A \pi^2}{12} + (1-\delta_s)\frac{\mathcal{V}_g(\theta_*)}{4} \right];$$

$$\mathcal{C}_{g/a}^{(0)}(x) = \delta_{ga}\delta(1-x); \ \mathcal{C}_{g/g}^{(1,c)}(x) = \delta(1-x)(1-\delta_s)\frac{\mathcal{V}_g(\theta_*)}{4}; \ \mathcal{C}_{g/q_S}^{(1,c)}(x) = \frac{C_F}{2}x. \tag{A12}$$

These coefficients are taken from Refs. [12, 13, 44, 45].

Appendix B: COMPONENTS OF THE ASYMPTOTIC CROSS SECTIONS

In Sec. II B we introduce asymptotic small-Q_T approximations for the $q\bar{q}+qg$ and $gg+gq_S$ NLO cross sections,

$$A_{q\bar{q}}(Q, Q_T, y, \Omega_*) = \sum_{i=u,\bar{u},d,\bar{d},\dots} \frac{\Sigma_i(\theta_*)}{S} \left\{ \delta(\vec{Q}_T) F_{i,\delta}(Q, y, \theta_*) + F_{i,+}(Q, y, Q_T) \right\}, \tag{B1}$$

and

$$A_{gg}(Q, Q_T, y, \Omega_*) = \frac{1}{S}\left\{ \Sigma_g(\theta_*) \left[\delta(\vec{Q}_T) F_{g,\delta}(Q, y, \theta_*) + F_{g,+}(Q, y, Q_T) \right] \right.$$

$$\left. + \Sigma'_g(\theta_*, \varphi_*) F'_g(Q, y, Q_T) \right\}. \tag{B2}$$

The functions F in these equations are defined as

$$F_{i,\delta}(Q, y, \theta_*) \equiv f_{q_i/h_1}(x_1, \mu_F) f_{\bar{q}_i/h_2}(x_2, \mu_F) \left(1 + 2\frac{\alpha_s}{\pi} h_q^{(1)}(\theta_*) \right)$$

$$+ \frac{\alpha_s}{\pi}\left\{ \left(\left[\mathcal{C}_{q_i/a}^{(1,c)} \otimes f_{a/h_1} \right](x_1, \mu_F) - \left[P_{q_i/a} \otimes f_{a/h_1} \right](x_1, \mu_F) \ln\frac{\mu_F}{Q} \right) f_{\bar{q}_i/h_2}(x_2, \mu_F) \right.$$

$$\left. + f_{q_i/h_1}(x_1, \mu_F) \left(\left[\mathcal{C}_{\bar{q}_i/a}^{(1,c)} \otimes f_{a/h_2} \right](x_2, \mu_F) - \left[P_{\bar{q}_i/a} \otimes f_{a/h_2} \right](x_2, \mu_F) \ln\frac{\mu_F}{Q} \right) \right\}; \tag{B3}$$

$$F_{q,+} = \frac{1}{2\pi}\frac{\alpha_s}{\pi}\left\{ f_{q_i/h_1}(x_1, \mu_F) f_{\bar{q}_i/h_2}(x_2, \mu_F) \left(\mathcal{A}_q^{(1,c)} \left[\frac{1}{Q_T^2} \ln\frac{Q^2}{Q_T^2} \right]_+ + \mathcal{B}_q^{(1,c)} \left[\frac{1}{Q_T^2} \right]_+ \right) \right.$$

$$+ \left[\frac{1}{Q_T^2} \right]_+ \left(\left[P_{q_i/a} \otimes f_{a/h_1} \right](x_1, \mu_F) f_{\bar{q}_i/h_2}(x_2, \mu_F) \right.$$

$$\left.\left. + f_{q_i/h_1}(x_1, \mu_F) \left[P_{\bar{q}_i/a} \otimes f_{a/h_2} \right](x_2, \mu_F) \right) \right\}; \tag{B4}$$

$$F_{g,\delta} \equiv f_{g/h_1}(x_1, \mu_F) f_{g/h_2}(x_2, \mu_F) \left(1 + 2\frac{\alpha_s}{\pi} h_g^{(1)}(\theta_*) \right)$$

$$+ \frac{\alpha_s}{\pi}\left\{ \left(\left[\mathcal{C}_{g/a}^{(1,c)} \otimes f_{a/h_1} \right](x_1, \mu_F) - \left[P_{g/a} \otimes f_{a/h_1} \right](x_1, \mu_F) \ln\frac{\mu_F}{Q} \right) f_{g/h_2}(x_2, \mu_F) \right.$$

$$\left. + f_{g/h_1}(x_1, \mu_F) \left(\left[\mathcal{C}_{g/a}^{(1,c)} \otimes f_{a/h_2} \right](x_2, \mu_F) - \left[P_{g/a} \otimes f_{a/h_2} \right](x_2, \mu_F) \ln\frac{\mu_F}{Q} \right) \right\}; \tag{B5}$$

$$F_{g,+} = \frac{1}{2\pi}\frac{\alpha_s}{\pi}\left\{ f_{g/h_1}(x_1, \mu_F) f_{g/h_2}(x_2, \mu_F) \left(\mathcal{A}_g^{(1,c)} \left[\frac{1}{Q_T^2} \ln\frac{Q^2}{Q_T^2} \right]_+ + \mathcal{B}_g^{(1,c)} \left[\frac{1}{Q_T^2} \right]_+ \right) \right.$$

$$+ \left[\frac{1}{Q_T^2} \right]_+ \left(\left[P_{g/a} \otimes f_{a/h_1} \right](x_1, \mu_F) f_{g/h_2}(x_2, \mu_F) \right.$$

$$\left.\left. + f_{g/h_1}(x_1, \mu_F) \left[P_{g/a} \otimes f_{a/h_2} \right](x_2, \mu_F) \right) \right\}; \tag{B6}$$

and

$$F'_{g,+} = \frac{1}{2\pi}\frac{\alpha_s}{\pi} \left[\frac{1}{Q_T^2} \right]_+ \left(\left[P'_{g/g} \otimes f_{g/h_1} \right](x_1, \mu_F) f_{g/h_2}(x_2, \mu_F) \right.$$

$$\left. + f_{g/h_1}(x_1, \mu_F) \left[P'_{g/g} \otimes f_{g/h_2} \right](x_2, \mu_F) \right) \right\}. \tag{B7}$$

Expressions for the coefficients $\mathcal{A}_a^{(1,c)}, \mathcal{B}_a^{(1,c)}, h_a^{(1)}(\theta_*), \mathcal{C}_{a/a'}^{(1,c)}(x)$, and splitting functions $P_{a/c}(x)$, are listed in Appendix A. Summation over all relevant parton flavors $a' = g, u, \bar{u}, d, \bar{d}, \ldots$ for $a = q$ and $a' = g, q_S$ for $a = g$ is assumed. In addition, the φ_*-dependent part $\Sigma'_g(\theta_*, \varphi_*) F'_g(Q, y, Q_T)$ of the $gg + gq_S$ asymptotic cross section A_{gg} contains a splitting function

$$P'_{gg}(x) = 2C_A(1-x)/x, \tag{B8}$$

contributed by the interference of splitting amplitudes with opposite gluon polarizations in the helicity amplitude formalism [46, 47, 48, 49]. The origin and behavior of this spin-flip function are discussed in Ref. [3].

[1] D. Acosta et al. (CDF Collaboration), Phys. Rev. Lett. **95**, 022003 (2005).
[2] C. Balazs, E. L. Berger, P. Nadolsky, and C. P. Yuan, Phys. Lett. **B637**, 235 (2006).
[3] P. Nadolsky, C. Balazs, E. Berger, and C. P. Yuan (2007), hep-ph/0702003.
[4] P. Aurenche, A. Douiri, R. Baier, M. Fontannaz, and D. Schiff, Z. Phys. **C29**, 459 (1985).
[5] B. Bailey, J. F. Owens, and J. Ohnemus, Phys. Rev. **D46**, 2018 (1992).
[6] E. L. Berger, E. Braaten, and R. D. Field, Nucl. Phys. **B239**, 52 (1984).
[7] C. Balazs, P. Nadolsky, C. Schmidt, and C.-P. Yuan, Phys. Lett. **B489**, 157 (2000).
[8] D. de Florian and Z. Kunszt, Phys. Lett. **B460**, 184 (1999).
[9] Z. Bern, A. De Freitas, and L. J. Dixon, JHEP **09**, 037 (2001).
[10] Z. Bern, L. J. Dixon, and C. Schmidt, Phys. Rev. **D66**, 074018 (2002).
[11] J. C. Collins, D. E. Soper, and G. Sterman, Nucl. Phys. **B250**, 199 (1985).
[12] C. Balazs, E. L. Berger, S. Mrenna, and C.-P. Yuan, Phys. Rev. **D57**, 6934 (1998).
[13] P. M. Nadolsky and C. R. Schmidt, Phys. Lett. **B558**, 63 (2003).
[14] T. Binoth, J. P. Guillet, E. Pilon, and M. Werlen, Eur. Phys. J. **C16**, 311 (2000).
[15] J. C. Collins and D. E. Soper, Phys. Rev. **D16**, 2219 (1977).
[16] J. C. Collins and D. E. Soper, Nucl. Phys. **B197**, 446 (1982).
[17] J. C. Collins and D. E. Soper, Nucl. Phys. **B193**, 381 (1981).
[18] A. V. Konychev and P. M. Nadolsky, Phys. Lett. **B633**, 710 (2006).
[19] J. Pumplin et al., JHEP **07**, 012 (2002).
[20] S. Berge, P. Nadolsky, F. Olness, and C.-P. Yuan, Phys. Rev. **D72**, 033015 (2005).
[21] S. Catani, D. de Florian, and M. Grazzini, Nucl. Phys. **B596**, 299 (2001).
[22] E. L. Berger, X. Guo, and J. Qiu, Phys. Rev. **D54**, 5470 (1996).
[23] S. Catani, M. Fontannaz, and E. Pilon, Phys. Rev. **D58**, 094025 (1998).
[24] S. Catani, M. Fontannaz, J. P. Guillet, and E. Pilon, JHEP **05**, 028 (2002).
[25] S. Frixione, Phys. Lett. **B429**, 369 (1998).
[26] S. Catani and M. H. Seymour, Nucl. Phys. **B485**, 291 (1997).
[27] E. L. Berger, L. E. Gordon, and M. Klasen, Phys. Rev. **D58**, 074012 (1998).
[28] E. L. Berger, J. Qiu, and X. Zhang, Phys. Rev. **D65**, 034006 (2002).
[29] G. A. Ladinsky and C.-P. Yuan, Phys. Rev. **D50**, 4239 (1994).
[30] F. Landry, R. Brock, P. M. Nadolsky, and C. P. Yuan, Phys. Rev. **D67**, 073016 (2003).
[31] C. Balazs and C.-P. Yuan, Phys. Rev. **D56**, 5558 (1997).
[32] C. Balazs (1999), hep-ph/9906422.

[33] S. Eidelman et al. (Particle Data Group), Phys. Lett. **B592**, 1 (2004).

[34] L. Bourhis, M. Fontannaz, and J. P. Guillet, Eur. Phys. J. **C2**, 529 (1998).

[35] J. Dyer, private communication.

[36] E. L. Berger and J. Qiu, Phys. Rev. **D67**, 034026 (2003).

[37] ATLAS Collaboration, *ATLAS detector and physics performance. Technical design report. Vol. 2* (1999), CERN-LHCC-99-15.

[38] C. Balazs and C.-P. Yuan, Phys. Lett. **B478**, 192 (2000).

[39] S. Catani, D. de Florian, M. Grazzini, and P. Nason, JHEP **07**, 028 (2003).

[40] G. Bozzi, S. Catani, D. de Florian, and M. Grazzini, Nucl. Phys. **B737**, 73 (2006).

[41] D. Binosi and L. Theussl, Comput. Phys. Commun. **161**, 76 (2004).

[42] D. de Florian and M. Grazzini, Phys. Rev. Lett. **85**, 4678 (2000).

[43] S. Moch, J. A. M. Vermaseren, and A. Vogt, Nucl. Phys. **B688**, 101 (2004).

[44] C.-P. Yuan, Phys. Lett. **B283**, 395 (1992).

[45] A. Vogt, S. Moch, and J. A. M. Vermaseren, Nucl. Phys. **B691**, 129 (2004).

[46] Z. Bern, L. J. Dixon, and D. A. Kosower, Phys. Rev. Lett. **70**, 2677 (1993).

[47] Z. Bern, G. Chalmers, L. J. Dixon, and D. A. Kosower, Phys. Rev. Lett. **72**, 2134 (1994).

[48] Z. Bern, L. J. Dixon, D. C. Dunbar, and D. A. Kosower, Nucl. Phys. **B425**, 217 (1994).

[49] Z. Bern, L. J. Dixon, and D. A. Kosower, Nucl. Phys. **B437**, 259 (1995).